Geomechanics for Energy and the Environment 42 (2025) 100654

Contents lists available at ScienceDirect

Geomechanics for Energy and the Environment

journal homepage: www.elsevier.com/locate/gete

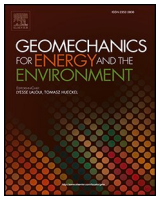

A comparative analysis of numerical approaches for the description of gas flow in clay-based repository systems: From a laboratory to a large-scale gas injection test

E. Tamayo-Mas [a,*], J.F. Harrington [a], I.P. Damians [b], J.T. Kim [c], E. Radeisen [d], J. Rutqvist [e], C. Lee [c], B.S. Noghretab [b], R.J. Cuss [a]

[a] British Geological Survey, Keyworth, Nottingham, United Kingdom
[b] International Centre for Numerical Methods in Engineering (CIMNE), Universitat Politècnica de Catalunya·BarcelonaTech (UPC), Barcelona, Spain
[c] Korea Atomic Energy Research Institute, Daejeon, South Korea
[d] Federal Institute for Geosciences and Natural Resources, Hanover, Germany
[e] Lawrence Berkeley National Laboratory, Berkeley, CA, USA

ARTICLE INFO

Keywords:
Upscaling
Dilatancy-controlled gas flow
Enhanced numerical hydro-mechanical models
Comparative study
Bentonite gas tests
DECOVALEX

ABSTRACT

There is nowadays a consensus among many countries that geological disposal is a favourable solution for the long-term management. Although different host formations and different barrier systems are under consideration around the world, clay-based materials form an important component for waste isolation in most national programmes. Hence, a good comprehension of the effect of gas flow on the hydro-mechanical behaviour of clay-based soils is essential, both at laboratory and field scale. Task B under the international cooperative project DECOVALEX-2023 has recently shown that, after some enhancement, models can be employed to reproduce laboratory scale tests, even with different sample geometries[37]. However, further work is required to understand whether they can be applied to simulate a large-scale experiment. Up-scaling of models for the advective transport of gas through clay-based low permeable material presents a number of problems related to the difficulty in obtaining consistent hydrogeological parameters and constitutive relationships at both laboratory and field scale. Based on a unique dataset from a large-scale gas injection test (Lasgit) performed at the Äspö Hard Rock Laboratory (Sweden), Task B within DECOVALEX-2023 has explored the refinement of these numerical strategies applied to the simulation of gas flow. Work performed within the task reveals that codes do not need to be substantially modified from the laboratory models to reproduce full-scale tests: indeed, model parameters calibrated and validated at laboratory scale have been applied to predict field scale gas flow at Lasgit, including peak gas pressure and injected cumulative gas volume. By means of (1) the introduction of interfaces between blocks to reflect the experimental configuration and the (2) adjustment of some parameters (e.g., higher permeability), the updated models are able to represent most of the key features observed in the experimental data, even at a large scale.

1. Introduction

There is nowadays consensus among many countries that geological disposal is a favourable solution for the long-term management of intermediate- and high-level radioactive waste[32]. Although, worldwide, different host formations and different barrier systems are being considered, clay-based materials are of interest in most national programmes[20]. Their properties (e.g., low permeability, strong contaminant retention and self-sealing capacity) make them excellent candidates as potential host formations and/or as parts of an engineered barrier system. Thus, a solid understanding of the long-term performance of clay-based materials is needed.

A key issue in the advancement of clay-based materials' understanding concerns a good comprehension of their mechanical and

* Corresponding author.
E-mail addresses: elena@bgs.ac.uk (E. Tamayo-Mas), jfha@bgs.ac.uk (J.F. Harrington), ivan.puig@upc.edu (I.P. Damians), kjt@kaeri.re.kr (J.T. Kim), eike.radeisen@bgr.de (E. Radeisen), jrutqvist@lbl.gov (J. Rutqvist), leecs@kaeri.re.kr (C. Lee), babak.sayad.noghretab@upc.edu (B.S. Noghretab), rjcu@bgs.ac.uk (R.J. Cuss).

https://doi.org/10.1016/j.gete.2025.100654
Received 15 July 2024; Received in revised form 11 February 2025; Accepted 19 February 2025
Available online 22 February 2025

hydraulic response in the presence of free gas. Indeed, radioactive waste hosted in very low permeability formations can generate a significant amount of gas as a result of the corrosion of metallic materials under anoxic conditions, the radioactive decay of waste and the radiolysis of water. If the gas production rate exceeds the diffusive capacity of the clay, a discrete gas phase will form, which continues to accumulate until its pressure becomes large enough to exceed the entry pressure of the surrounding material. At this point, advective flow of gas is expected to occur. There is now a substantial body of evidence, spanning multiple decades, indicating that in these materials, gas migration occurs through the creation of dilatant pathways rather than by moving within the original porosity of the clay as conceptualised in Darcy's law (see for instance[15,13,14,6] and[7]). Hence, the complex hydro-mechanical coupling[11,12,34] introduced by the interaction of these pathways with the surrounding clay needs to be fully understood.

To this end, in recent years, a substantial amount of both experimental and modelling work has been performed as part of numerous international projects[18,19]. The DECOVALEX (DEvelopment of COupled Models and VALidation against EXperiments) Project is one of these international research collaboration exercises that has recently focused on the description and further understanding of the highly non-linear gas migration process observed in very low permeability formations. In its last phase (Task A within DECOVALEX-2019, see[35]), participating teams developed advanced modelling approaches using different numerical methods and computer codes to model the movement of gas in a number of controlled laboratory experiments[11,9]. These enhanced approaches appeared capable of reproducing some of the observed experimental behaviours (e.g., experimental stress and pore pressure measurement results). However, they remained unable to describe the full complexity of the physical processes observed in water-saturated experiments (e.g., creation of discrete dilatant pathways). To this end, several concerns were raised in Task A DECOVALEX-2019 reflecting the fact some key features in the modelling of advective gas (e.g., parameter calibration and model constraints, heterogeneity, stochasticity and upscaling) were still unclear. Hence, the primary focus of Task B within the current phase of the project (DECOVALEX-2023) has been on the further refinement and enhancement of these numerical strategies.

Task B under DECOVALEX-2023 has shown that, after enhancement, models that were used can simulate multiple laboratory scale experiments, even with different sample geometries[36]. The study has also shown that (i) these numerical approaches can successfully represent some of the main deterministic experimental features typically observed in dilatancy-controlled gas flow (e.g., initial and peak stress values) and that (ii) some other features (e.g., rapid transition phase seen at breakthrough) are still not correctly captured, at least at the laboratory scale. Further work is therefore required to understand whether a similar behaviour is observed when applying the numerical approaches from the laboratory study to simulate a large-scale experiment. Indeed, modelling advective transport of gas through a very low permeable material at the field scale presents a number of problems because of the difficulty of obtaining consistent hydrogeological parameters and constitutive relationships at the appropriate scale. The applicability of upscaling conventional continuum models which do not explicitly represent the physics controlling gas flow in compact saturated bentonite from the micro to macro scale may be also questionable. Hence, work is needed to address these issues, in conjunction with the consideration of gas-water interactions. Task B, within DECOVALEX-2023, has further explored the refinement of these numerical strategies to the simulation of a large-scale gas injection test (Lasgit) performed at the Äspö Hard Rock Laboratory (Sweden). This was a highly instrumented test based on a mockup full scale canister, encapsulated in pre-compacted bentonite rings/pellets, and placed within a 2 m diameter deposition hole of 9 m depth.

The objective of Task B was to explore whether enhanced numerical approaches developed for laboratory scale experiments could also be employed to simulate a full-scale test. For this purpose, the Lasgit experiment (Section 2) was modelled by means of four enhanced numerical approaches (Section 3). Three of these approaches had been previously employed to describe different well-constrained laboratory experiments[36]. Special emphasis has been placed on the modifications that had to be made when simulating the full-scale test. Numerical capabilities are then assessed, and their performance is analysed in Section 4. Finally, a discussion of main findings and key conclusions are provided in Sections 5 and 6 respectively.

2. Experimental data: the large-scale gas injection test (Lasgit)

Models and codes developed to simulate laboratory scale experiments have been employed to numerically reproduce one of the gas injection experiments (gas injection test 4) performed as a part of the Lasgit project (LArge-Scale Gas Injection Test), see Fig. 1. Lasgit was a full-scale demonstration experiment operated by The Swedish Nuclear Fuel and Waste Management Company (SKB) at the Äspö Hard Rock Laboratory at a depth of 420 m, with the two main objectives of providing quantitative data to improve process understanding and validating numerical approaches used in safety assessment, see Cuss et al.[7] for a detailed description of this 17-year project. The experiment started (Day 0) on 1st February 2005 with the closure of the deposition hole and the start of the hydration stage.

2.1. Experimental setup

The Lasgit experiment was commissioned in a deposition hole (DA3147G01) with a length of ~8.5 m and diameter of ~1.75 m. A full-scale KBS-3 copper canister with iron insert was modified with thirteen circular filters of varying dimensions located on its surface in three separate arrays (see Fig. 2), to provide point sources for gas injection simulating potential canister defects. These filters could also be used to inject water during the hydration stages to help locally saturate the buffer around each test filter. Filter mats were placed in strategic positions both within the buffer and on the rock-wall to aid hydration. The canister was surrounded by specially manufactured pre-compacted bentonite blocks (~ 25 tonnes total), with initial water saturations >95 %. In the engineering void between the pre-compacted bentonite rings and the rock-wall, bentonite pellets were used. As the bentonite system began to saturate these swelled to fill the construction gaps and formed a seal around the canister. The emplacement hole was capped by a conical concrete plug retained by a reinforced SS2172 carbon steel lid capable of withstanding over 5000 kN force.

The deposition hole, buffer, and canister were equipped with instrumentation to measure the total stress (PR, PB, PC), pore-water pressure (UR, UB), and relative humidity (WR) in 32, 26 and 7 positions respectively (see Fig. 2 for sensor locations). Additional instrumentation continually monitored variations in temperature, relative displacement of the lid and canister, and the restraining forces on the rock anchors. The experiment was monitored and controlled from a temperature-controlled gas laboratory that allowed remote control and monitoring of the test. A full description of the experimental setup is given in Cuss et al.[7].

The boundary conditions of the experiment were those dictated by the pressures and stresses built up within the bentonite buffer during rehydration. The canister lid had been pre-stressed to 1300 kN to impose a similar force comparable with that which would be generated by the back-fill placed within the gallery above each deposition hole in a geological disposal facility. The experiment was conducted at ambient temperatures.

2.2. Test history

Gas injection test 4 started on day 2726.08 (20th July 2012) and was completed at day 3283.06 (26th January 2014), lasting for a total stage time of 556.98 days. It was the third gas injection test conducted in filter

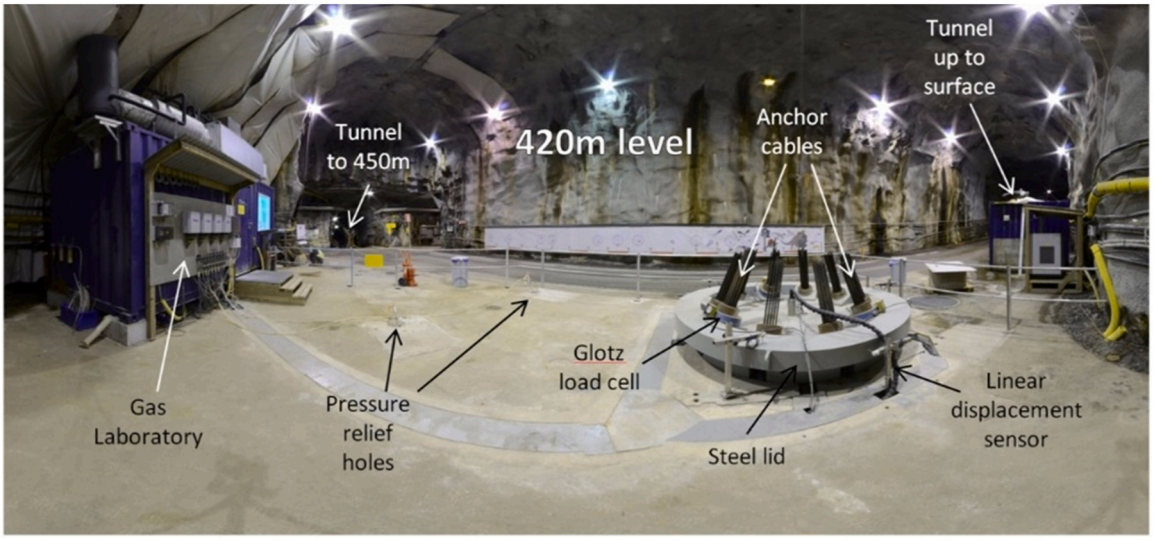

Fig. 1. A panoramic view of the Large-scale gas injection test (Lasgit) 420 m below ground at the Äspö Hard Rock Laboratory in Sweden (from[7]). The blue container on the left housed the artificial hydration and gas injection systems which were connected into the borehole along channels cut into the gallery floor. The lid and rock anchors of the deposition hole can be seen into the centre right.

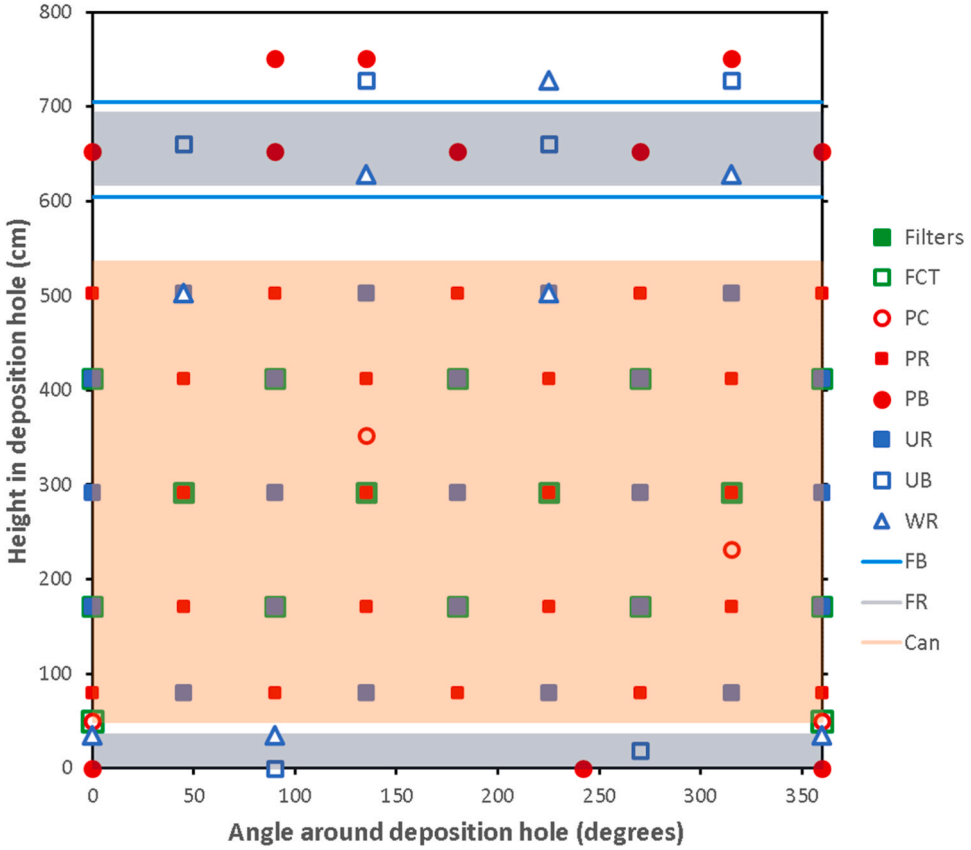

Fig. 2. Map of the deposition hole wall showing the location of all sensors. Note: FCT = full canister test filter; PC = total stress sensor on canister surface; PR = total stress sensor at rock wall; PB = total stress sensor within the buffer; UR = pore water pressure at the rock wall; UB = pore water pressure within the buffer; WR = relative humidity; FB = filter mat between bentonite segments; FR = filter mat at the rock wall; Can = position of the canister. See Cuss et al.[7] for detailed map of sensor locations.

FL903, located on the lower array of filters on the canister surface. Filter FL903 was 50 mm diameter, made of sintered bronze with an average pore size of 4–8 μm. The test comprised two stages: (1) a two-stage hydraulic test to determine the hydraulic properties of the bentonite at filter FL903 lasting approximately 60 days and (2) a gas injection test, where gas pressure was raised from background levels up to gas peak pressure using a four-stage ramp, being held at constant pressure in between, which is the focus of the modelling exercise.

Fig. 3 shows a simplified schematic of the gas test setup. Approximately 3750 ml of helium was added to a stainless steel interface vessel,

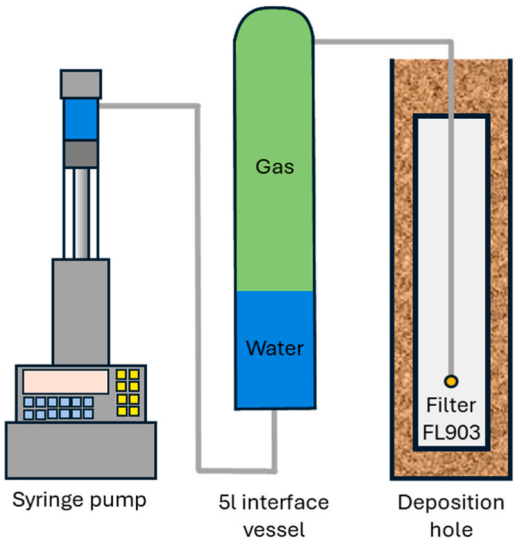

Fig. 3. Simplified schematic of the gas injection system.

located within the Lasgit gas laboratory (Fig. 1) at a starting pressure of 1868 kPa. The injection filter was thoroughly flushed of water using pressurised helium and the drain from filter FL903. Once flushed, it was common for flow to take a few days to stabilise as gas went into solution and any remaining water within the filter was expelled into the bentonite. The first pressure ramp was started at day 2988.07 (8th April 2013) by the injection of water into the base of the interface vessel at a rate of 2.45 ml h^{-1}. This raised pressure from 1868 to 2867 kPa in 23.9 days, as shown in Fig. 4, when pressure control was switched to constant pressure from day 3011.99 for 26.0 days. Injection of water into the interface vessel is required to maintain constant gas pressure as gas moves into solution or through diffusive processes. The second pressure ramp was started at day 3038.04 on (28th May 2013) by the injection of water into the base of the interface vessel at a rate of 1.2 ml h^{-1}. This raised pressure from 2868 to 3856 kPa in 23.1 days, after which pressure was held constant from day 3061.17 for 26.1 days. The third pressure ramp was started at day 3087.24 (16th July 2013) by the injection of water into the base of the interface vessel at a rate of 0.725 ml h^{-1}. This raised pressure from 3867 to 4852 kPa in 23.2 days, after which pressure was held constant from day 3110.48 for 52.6 days. The fourth, and final, pressure ramp was started at day 3163.04 (30th September 2013) by the injection of water into the base of the interface vessel at a rate of 0.35 ml h^{-1}. This raised pressure from 4854.01 to a gas peak pressure of 6174 kPa at day 3205.31, 42 days after the start of the fourth pressure ramp. The injection of water into the base of the interface vessel continued at 0.35 ml h^{-1}, until day 3235.13 when flow was reduced to 0.175 ml h^{-1}, and day 3256.19 when it was reduced further to 0.088 ml h^{-1}. Injection was stopped at day 3283.02 (28th January 2014) and in total, 2910.5 ml of water was injected into the base of the interface vessel. For a detailed description of each gas ramp, the authors refer to the Lasgit final report by Cuss et al.[7].(Table 1)

2.3. Results

Fig. 4 shows the calculated flow of gas into the system and into the clay at STP. Flow into the system at STP is calculated from the flowrate of water into the interface vessel, while flow into the clay is derived from the difference in observed gas pressure to the predicted gas pressure assuming the ideal gas law. The STP flow rate into the system reduced between each successive gas ramp. Flow into the clay was seen in each ramp, with little flow observed during periods of constant pressure. Table 2 summarises all the flow data from the four pressure ramps, detailing the range of STP flow and quantity of gas entering the buffer seen during the pressure ramp, and the pressure of the constant pressure step and the resultant STP flow into the clay. For gas ramp 4 the latter shows the peak gas pressure and the peak in flow into the buffer.

During gas ramp 4, significant gas entry was seen to begin at day

Table 1
Initial conditions prescribed for the simulation of the hydration phase.

Pressure ramp	Pressure ramp		Pressure hold	
	STP flow into clay	Gas entering clay	Pressure hold/ peak pressure	STP flow into clay
	$\times 10^{-9}$ m^3 s^{-1}	mol	kPa	$\times 10^{-11}$ m^3 s^{-1}
1	12.5 – 14.8	0.10	2867	5.75
2	9.3 – 12.4	0.12	3860	13.7
3	7.51 – 9.41	0.13	4853	25.9
4	4.52 – 5.71	0.21	6174	3270 (peak)

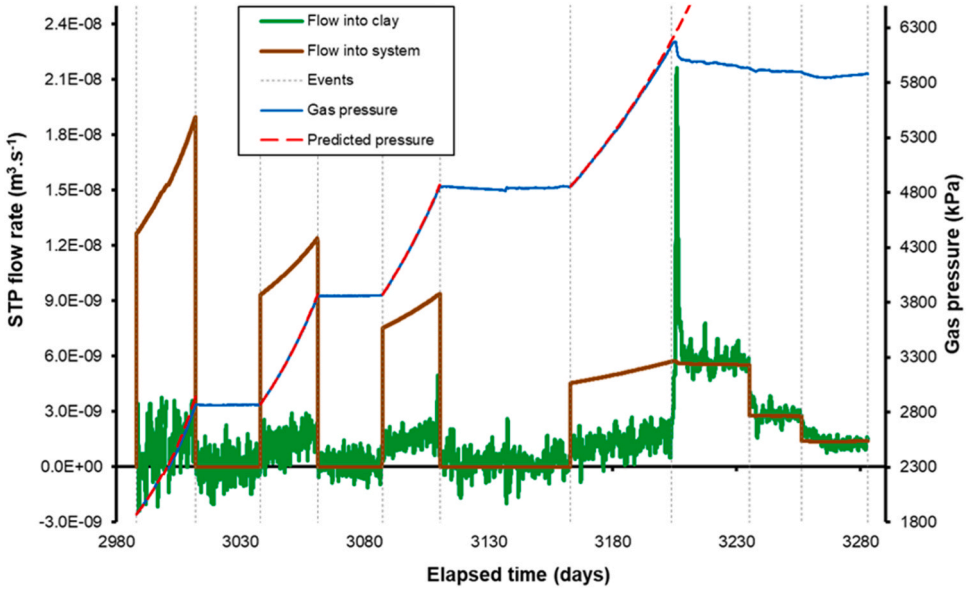

Fig. 4. Recorded and predicted gas pressure, and flow of gas into the system and the clay during Gas Test 4 (from[7]).

Table 2
Initial conditions prescribed for the simulation of the hydration phase.

	Bentonite (pre-compacted blocks, swollen bentonite and interfaces)	Injection filter	Rock and copper canister wall
Capillary pressure	3 – 0.4 MPa	3 – 0.4 MPa	3 MPa
Effective stresses	σ_{xx} = 3.23 MPa σ_{yy} = 3.23 MPa σ_{zz} = 3.73 MPa	σ_{xx} = 0 MPa σ_{yy} = 0 MPa σ_{zz} = 0 MPa	σ_{xx} = 4.23 MPa σ_{yy} = 4.23 MPa σ_{zz} = 4.73 MPa
Gas pressure	2.4 MPa	1.85 MPa	2.4 MPa

3203.73, as seen by an increase in flow rate into the clay. This resulted in a single peak in flow of 3.27×10^{-8} m^3 s^{-1} at day 3205.72. The peak in flow was short-lived with flow into the clay matching flow into the system within four days. From then afterwards the flow into the clay was slightly greater than the flow into the system, giving a slow reduction in gas pressure. As gas pressure reduction appeared steady, the flow rate of the injection pump was lowered in two steps, approximately halving flow at each step. As before, flow into the clay approximated flow into the system, with slightly higher flow into the clay resulting in the continued reduction in gas pressure. However, in the final stage the flow into the clay reduced, resulting in an increase in gas pressure. Following gas entry, a total of 1.13 mol entered the clay.

As also seen in the laboratory-scale test (see[36]), there exists a pronounced coupling between pore water pressures at the rock wall and gas entry (see Fig. 5). Indeed, at day 3203.73 (when flow accelerated), an event was seen in UR905 and UR908; pore pressure at the rock wall. This occurred at a gas pressure of 6141 kPa. At day 3204.66, pore pressure at UR908 showed a stepped increase of around 12 kPa and radial stress at the rock wall at PR907 and PR908 started to increase, as did flow into the clay. At day 3205.31, peak gas pressure occurred (at a pressure of 6174 kPa) resulting in a single peak in flow of 3.27×10^{-8} m^3s^{-1} at day 3205.72. This peak in flow was short-lived with flow into the clay matching flow into the system within four days. From then onwards the flow into the clay was slightly greater than the flow into the system, giving a slow reduction in gas pressure. Soon after the peak event, at day 3205.88, pore pressure at UR905, UR907, and UR908 peaked. At day 3206.40, radial stress at PR905, PR906, and PR907 increased by 8.6, 28.6, and 9.6 kPa respectively, while PR909 decreased by 7.1 kPa. Stress at PR908 increased from day 3204.66 onwards and coincident with the changes seen in the other sensors reduced by ~5 kPa, before quickly recovering with a peak in stress ~15 kPa higher than the starting magnitude. Then, pore pressure remained relatively static, until day 3217.11, when some sensors (UR905, UR908, UR916 and UR919) showed small, short lived, reductions in pore pressure of ~4–10 kPa thus suggesting that gas flow was pulsed, see Cuss et al.[7] for a detailed description of these events. At day 3235.11, a decrease was seen in pore pressure at UR919, with disturbances in UR905, UR908, and UR916. Then, at day 3238.16, a 10 kPa step reduction in UR908 was followed by irregular pore pressure.

3. Modelling approaches

Four different numerical approaches have been adopted by BGR/UFZ (Federal Institute for Geosciences and Natural Resources and the Helmholtz Centre for Environmental Research), LBNL (Lawrence Berkeley National Laboratory), CIMNE-UPC/Andra (Universitat Politècnica de Catalunya funded by l'Agence nationale pour la gestion des des déchets radioactifs) and KAERI (Korea Atomic Energy Research Institute), see Appendix A for details about their key similarities and differences.

These four approaches are based on the general theory of multiphase flow modelling and are combined with additional features to describe some of the key aspects observed in both laboratory and field tests. The first three strategies had been previously employed to simulate laboratory scale tests and thus, their detailed description is not the aim of the present work, see the comparison paper by Tamayo-Mas et al.[36] for detailed features. Hence, in this study, a summary description is only given and emphasis is placed on the main conceptual modifications performed by the teams when upscaling. In contrast, a more detailed description of KAERI's approach is given.

3.1. Model developed by BGR/UFZ

3.1.1. Conceptual model

3.1.1.1. Mathematical model derived for the laboratory scale test. The gas-transport modelling approach selected by BGR/UFZ for the Lasgit test expands upon their previous work performed to simulate volumetrically constrained laboratory scale experiments. Indeed, BGR/UFZ developed a fully-coupled hydro-mechanical model based on multi-phase fluid flow theory (see[25]) to describe some of the key aspects observed in gas-laboratory tests. Their main features are:

- **Constitutive relations for the hydraulic and gas behaviour**: the Mualem model is adopted for the description of the relative permeabilities of gas and water whereas the relationship between water saturation and capillary pressure is based on the van Genuchten formulation[39].
- **Constitutive relations for the mechanical behaviour**: bentonite is assumed to behave as an elasto-plastic porous medium. Hooke's law

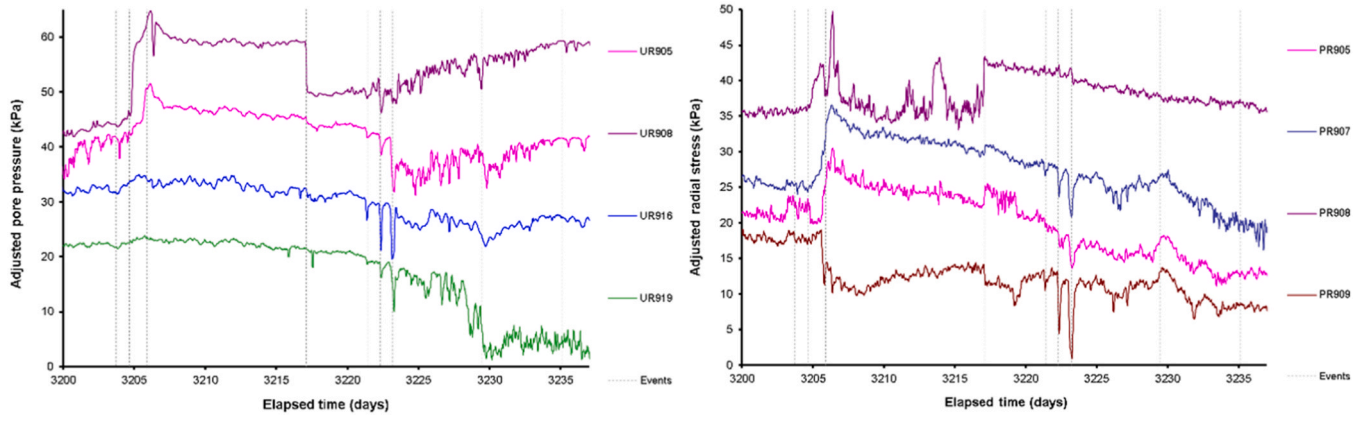

Fig. 5. Example of sensor response around the time of gas entry during Gas Injection Test 4. All parameters have had vertical shift to emphasise subtle detail. a) Pore pressure at the deposition wall; b) Radial stress on the deposition wall.

is assumed to describe the stress-strain relationship in the elastic regime of the material whereas the Drucker-Prager failure criterion is assumed to describe the plastic deformation (perfect plasticity with non-associated flow). This is enhanced with a tension cut-off parameter to limit the load carrying capacity of the model near the tensile region.

- **Hydro-mechanical coupling**: Biot's theory[2] is assumed to describe the hydro-mechanical coupling and hence, the effective stress tensor $\boldsymbol{\sigma}'$ (Pa) is calculated from the pore pressure $\mathbf{p}$ and the total stress tensor $\boldsymbol{\sigma}$ as

$$\boldsymbol{\sigma}' = \boldsymbol{\sigma} - \alpha \mathbf{p} \tag{1}$$

(where α (-) is the Biot's coefficient) and used to define the linear momentum balance equation of the porous medium

$$\nabla \left[\boldsymbol{\sigma}' - \alpha \left(p_g - S_w p_c \right) \mathbf{I} \right] + \rho \boldsymbol{g} = 0 \tag{2}$$

being p_g (Pa) the gas pressure, S_w (-) the water saturation, p_c (Pa) the capillary pressure, $\mathbf{I}$ the identity tensor, ρ (kg/m^3) the total density and $\boldsymbol{g}$ (m/s^2) the gravitational acceleration. The typical sign convention of rock mechanics is used for stresses, where a positive sign stands for compression and a negative sign for extension.

To allow localisation of gas flow, this continuous model is combined with an empirical strain-dependent permeability approach[41] that is extended with spatially distributed heterogeneous material properties, namely the Young's modulus and gas entry pressure.

3.1.1.2. Main conceptual modifications: from the laboratory to the field scale model. No significant conceptual changes have been made to the previous model to simulate the full-scale test. The main theoretical adjustment concerns the technique used to incorporate heterogeneity into the model. Although in the Lasgit modelling exercise, the formation of preferential pathways is less affected by the heterogeneous spatial distributions, the technique to derive heterogeneous Young's modulus values has been modified in order to represent micro-structures. Indeed, when simulating the laboratory scale test, a Gaussian normal distribution was assumed to derive the spatial distributions. Instead, in the full-scale modelling exercise, a pore-size-dependent (PSD) stochastic approach of the gas entry pressure has been derived from Mercury Intrusion Porosimetry. The PSD functions of comparable materials (MX-80 bentonite) have been used to identify the dominant pore modes and to analyse the porosity and void ratio in the structure[31]. This has been done using the Young-Laplace equation[10], which allows the description of the capillary pressure as a function of the pore throat width/radius via the relationship

$$p_c = \frac{2T_s \cos(\theta)}{a} \tag{3}$$

where T_s (=0.072 N/m) is the surface tension of the wetting fluid, θ is the angle between the wetting fluid and the solid phase and a is the radius of the pore throat. Assuming a constant state of quasi-full saturation $\left(\theta = 0^\circ,\ p_c = \frac{2T_s}{a} \right)$ and taking into account that the gas entry pressure corresponds to the gas pressure that must be applied for the gas phase to enter the pore space ($p_{entry} = p_{gas}$), Eq. (3) leads to

$$p_{entry} = p_{gas} = p_c + p_w = \frac{2T_s}{a} + p_w \tag{4}$$

Thus, in this model, the gas entry pressure is assumed to depend on the radius of the pore throat and the water pressure. Note that pathways are thought to be circular. This is an assumption, as pathways can be planar, thus impacting the description of the gas movement. Then, using the PSD of the fully saturated compacted bentonite (Fig. 6A), relative proportions of pore sizes can be estimated and the probability density of gas entry pressure (Fig. 6B) and hence, Young's modulus, can be derived.

3.1.2. Model geometry and numerical software

A 3D finite element model has been developed to represent experimental results of the gas injection test conducted in 2012. The open-source software OpenGeoSys (OGS - version 5.8) has been used, see Kolditz et al.[17].

To simulate the test, a hexahedral mesh of one quarter of the bentonite hollow cylinder has been employed, Fig. 7A. A height of 1.5 m has been considered and seven different material groups have been assumed, see Fig. 7B. Three of them have been used to describe the bentonite:

1. Three layers of pre-compacted MX-80 bentonite (named *bentonite blocks* in Fig. 7A).
2. The swollen bentonite (named *swollen bentonite* in Fig. 7A). These selected areas have been filled with bentonite pellets or have been left open before the hydration. For this group of materials, similar values were chosen as for the pre-compacted bentonite, but with

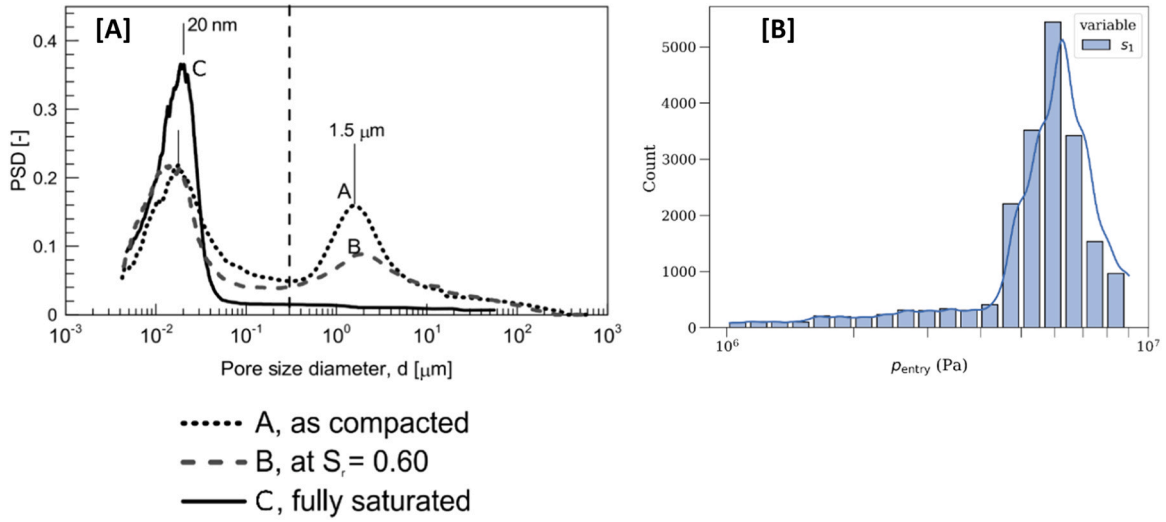

Fig. 6. [A] Pore size density in relation to different pore size diameters for three states: compacted but dry (A) with equal amounts of micropores and macropores, compacted and partially saturated (B) with twice as many of micropores than macropores, and compacted and fully saturated state (C) with mainly micropores (edited after Seiphoori[31]) and [B] Probability density of gas entry pressure in the bentonite materials.

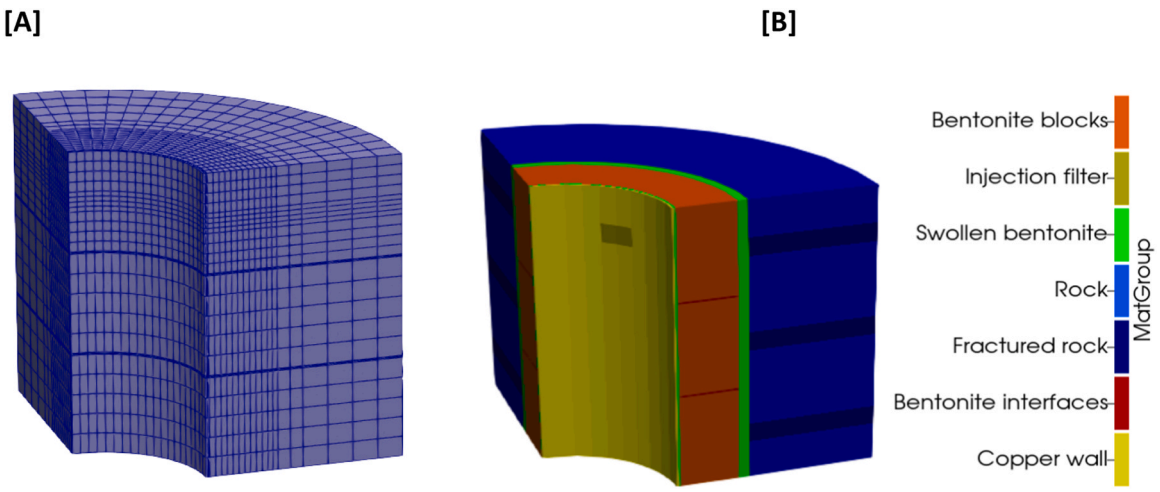

Fig. 7. [A] Mesh (with 21840 hexahedron elements and 24354 nodes) used by BGR/UFZ to simulate the Lasgit test and [B] geometry with the seven material groups considered.

some changes due to the reduction of the dry density as a result of the swelling.

3. An interface (named *bentonite interfaces* in Fig. 7A) between the bentonite blocks with the same properties as the bentonite blocks, but zero tensile strength.

Four other materials (with a high Young's modulus of E = 1000 GPa) have been considered to describe

4. The solid rock (named *rock* in Fig. 7A), with a very low permeability ($k = 1\times10^{-25}$ m²) and high mechanical strength.
5. The fractured rock on the outside of the model, with $k = 1\times10^{-18}$ m².
6. The injection filter, with a permeability of $k = 1\times10^{-16}$ m² and an initial gas volume of 2036 ml.
7. The copper wall.

3.1.3. Initial and boundary conditions

Prior to the gas injection test, the hydration phase (over the period from day 2100 to day 3100) has been simulated, with initial conditions of Table 2. Indeed, the swelling of the bentonite pellets and blocks has been modelled with respect to the change in stress and pressure. To account for swelling pressure in the bentonite, the linear swelling model proposed by Rutqvist et al.[29] has been assumed

$$\Delta\boldsymbol{\sigma}_{sw} = \boldsymbol{\sigma}_{sw,max}\Delta S_w \mathbf{I},\ \forall S_w \in [S_{res}, S_{max}] \tag{5}$$

where $\boldsymbol{\sigma}_{sw,max}$ (Pa) is the maximum swelling pressure, S_{res} (-) is the residual degree of saturation and S_{max} (-) is the maximum degree of saturation. This is considered to increase non-linearly with an increase of dry density. In particular, the empirical relationship for MX-80 bentonite

$$\boldsymbol{\sigma}_{sw,max} = 0.01e^{3.85\rho_d} \tag{6}$$

(established by[31]) has been employed.

During the hydration phase, the capillary pressure has been reduced from an initial value of 3 MPa to 0.4 MPa and the mean water saturation has been increased from $S_w = 0.9$ to $S_w = 0.998$. Subsequently, the gas injection has been applied with a Neumann boundary condition. The following boundary conditions have been assumed (see Fig. 8):

- Mechanical BC: $u_z = 0$ at top and bottom, $u_x = 0$ at the left and at inner and outer boundaries and $u_y = 0$ at the right and at inner and outer boundaries.
- Hydraulic BC: gas pressure has been prescribed at the bottom and at the outer boundaries ($p_g = 2$ MPa) and capillary pressure is prescribed at the outer boundaries ($p_c = 0.4$ MPa).

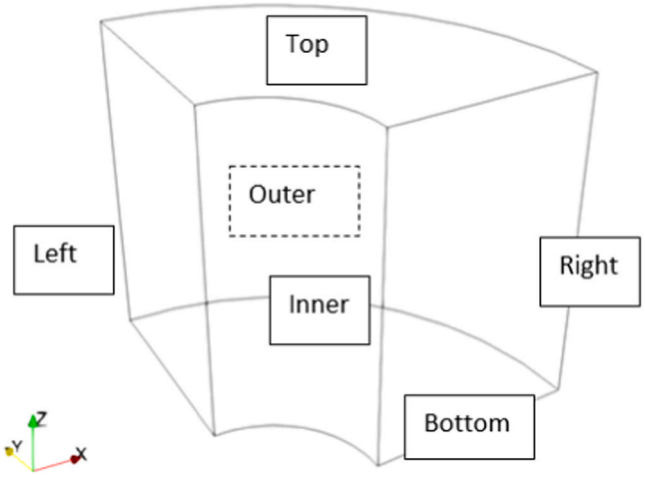

Fig. 8. Boundaries for the Lasgit modelling exercise.

3.2. Model developed by LBNL

3.2.1. Conceptual model

3.2.1.1. Mathematical model derived for the laboratory scale test. This full-scale approach builds upon LBNL's previous experience gained during the modelling of volumetrically constrained laboratory scale experiments[36]. Indeed, LBNL has developed an enhanced homogeneous continuum approach, which is based on the linking of the multiphase fluid flow simulator TOUGH2 with the commercial FLAC^{3D} geomechanical code thus enabling the simulation of processes characterised by strongly-coupled flow and geomechanics. The key features are:[28]

- **Constitutive relations for the hydraulic and gas behaviour**: as done by BGR/UFZ, the van Genuchten formulation is used to define the water retention curve. Relevant capillary pressure parameters for the bentonite are adopted from Senger and Marschall[33]. In this model, the modified Brooks-Corey relationships implemented in TOUGH2 relationships are adopted for the description of the relative permeabilities of gas and water. Following the approach by Senger and Marschall[33], an effective gas entry pressure was modeled through the application of a residual gas saturation considering the Brooks-Corey relative gas permeability.

- **Constitutive relations for the mechanical behaviour**: bentonite is assumed to behave as a linear elastic porous medium, with a volumetric swelling and a swelling stress that depends on the changes in water saturation ΔS_l according to

$$\Delta\sigma'_{sw} = \mathbf{K}\Delta S_l \beta_{sw} \tag{7}$$

where σ'_{sw} (Pa) is the swelling stress (with compression being positive), **K** (Pa) is the bulk modulus, S_l (-) is the liquid saturation and β_{sw} [-] is a calibrated moisture swelling coefficient (β_{sw} = 0.015), see Rutqvist et al.[29] for more details.

- **Hydro-mechanical coupling**: in this model, the effective stress tensor $\boldsymbol{\sigma}'$ (Pa) responds to the maximum phase pressure p^{ϕ} in the pore, that can be either gas pressure (if gas partially saturated) or liquid pressure (if fully water saturated):

$$\boldsymbol{\sigma}' = \boldsymbol{\sigma} - p^{\phi}\mathbf{I} \tag{8}$$

where again, $\boldsymbol{\sigma}'$ and $\boldsymbol{\sigma}$ are the effective and total stress tensors respectively (with compression being positive), **I** is the identity tensor and the pore pressure p^{ϕ} is defined as

$$p^{\phi} = \max(p_l, p_g) \tag{9}$$

with p_l and p_g liquid and gas phase pressures respectively.

To allow localisation of gas flow, this model assumes a fracture-like behaviour of the flow path. Hence, a pressure dependent permeability function

$$k = k_{\text{matrix}} + \frac{b_h^3}{12a} \tag{10}$$

is considered, where a [m] is the element width or spacing between dilatant flow paths, and b_h [m] is a non-linear function of the effective minimum compressive stress that reads

$$b_h = \frac{b_{h0}}{1 + 9\left(\frac{\sigma_n - P}{\sigma_{n,\,\text{ref}}}\right)} \tag{11}$$

with b_{h0} (m) being the (calibrated) maximum aperture for permeability, σ_n (Pa) the total stress normal to the fracture and $\sigma_{n,\,\text{ref}}$ (Pa) the reference stress normal to the fracture (calibrated from the laboratory experiments). The aperture versus pressure relationship of Eq. (11) corresponds to the Bandis et al.[1] model and its parameters need to be calibrated by matching pressure and outflow responses observed in the experiments. To be able to simulate the abrupt gas breakthrough response, the concept of a constant effective gas entry pressure was adopted by LBNL[28].

3.2.1.2. Main conceptual modifications: from the laboratory to the field scale model. As in the case of BGR/UFZ, no major conceptual changes have been made compared to the previous LBNL model when simulating the full-scale test. Interfaces were included into the model and simulated using same conceptual model as for bentonite block, but with some adjustments to the material properties. Indeed, interfaces are represented with a lower gas entry pressure (simulated with the residual gas saturation, Sgr) and a higher permeability value. Another conceptual adjustment concerns the technique used to describe the post-peak pressure behaviour. Here, assuming that dilatant flow paths can be represented as fracture-like elements, the capillary pressure of these elements has been scaled according to Olivella and Alonso[22] by the function of permeability as

$$P'_0 = P_0 \left(\frac{k_0}{k}\right)^{1/3} \tag{12}$$

where $\boldsymbol{P_0}$ is the initial van-Genuchten capillary pressure, $\boldsymbol{P'_0}$ is the corrected capillary pressure, $\boldsymbol{k}$ is the permeability and $\boldsymbol{k_0}$ is the initial permeability.

3.2.2. Model geometry and numerical software

A 3D symmetric model has been developed to represent Lasgit experimental results[28]. The simulator employed in this study was TOUGH-FLAC code[26,27,30], that combined the TOUGH2 multiphase flow simulator[24] with the commercial geomechanics code FLAC3D[16]. TOUGH2 enables the simulation of multiphase fluid flow and heat transport based on the integral finite difference method whereas FLAC3D is a finite-difference code that allows the representation of geomechanical features. Similar to other TOUGH-based geomechanical simulators, the two codes are sequentially coupled: in particular, fluid flow variables (such as pore pressure and saturation) calculated by TOUGH2 are transferred to FLAC3D, which then computes effective stresses and associated deformations, returning updated values for the stress-dependent permeability. The selection of small time-steps is important to find stable solutions of the hydraulic and mechanical response: a maximum time step of 1 day was prescribed while smaller time-steps (e.g., 100 seconds) were automatically calculated by TOUGH2 for convergence in the multiphase flow calculations around the gas breakthrough.

To simulate the gas injection test, the LBNL model assumed interfaces between (1) bentonite blocks, (2) the canister and the bentonite and (3) the rock and the bentonite, see Fig. 9.

3.2.3. Initial and boundary conditions

The system has initially been assumed to be fully saturated with bentonite and rock having a constant and uniform initial porewater pressure of 0.8 MPa. The initial stress conditions have been considered as 5 MPa in the radial and tangential directions and 6 MPa in the vertical direction. This initial stress reflects the initial stress in the bentonite caused by swelling after the saturation of the buffer. However, the same amount of initial stress is applied in the rock for this model simulation. Initial temperature is taken to be 15 ℃ and the initial pressure of the injector is 1868 kPa.

Regarding the boundary conditions, displacements normal to boundaries have been fixed to zero and gas injection has only been applied in one element of the canister mesh, which is connected to the bentonite. Water has been then injected into the gas filled injection element to compress the gas and raise the pressure according to the steps shown in the field. Due to the fact that only one half of the 3D geometry has been modelled, only one half of the injection filter and the injection rate has been simulated. The volume of the element has been calibrated in order to achieve a good match with the field data. The calibrated

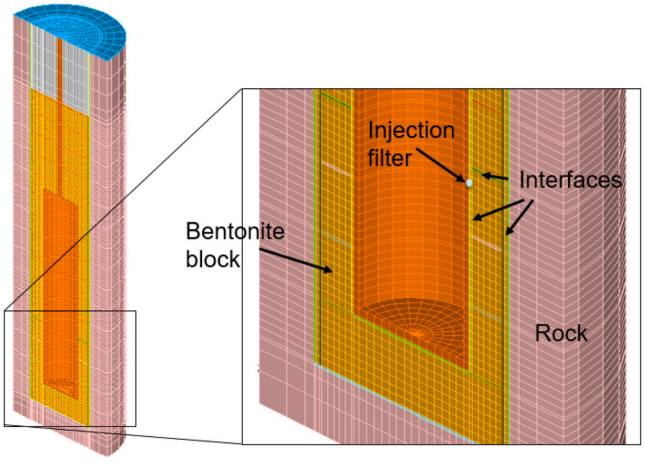

Fig. 9. Half-symmetric 3D model used to describe the Lasgit experiment. The model has 37,107 elements[28].

volume has been 2000 ml, thus meaning that the total injector volume (for the whole 3D specimen) has been calibrated to be 4000 ml, a slightly larger value than the quoted 3750 ml gas injection volume reported from the field. Thus, the volume was increased by 6 %, which was necessary to accurately match the stepwise injector pressure increase before gas breakthrough. The slightly higher gas volume can also have a slight impact on the gas pressure evolution after gas breakthrough.

3.3. Model developed by CIMNE-UPC/Andra

3.3.1. Conceptual model

3.3.1.1. Mathematical model derived for the laboratory scale test. The field scale technique is built on the work carried out by CIMNE-UPC/Andra when modelling laboratory scale experiments. CIMNE-UPC/Andra developed a coupled hydro-gas-mechanical 3D numerical model (see[8]), assuming a heterogeneous initial permeability field and embedded fractures[22]. This approach is characterised by the following key features:

- **Constitutive relations for the hydraulic and gas behaviour**: in the model developed by CIMNE-UPC/Andra, the retention curve is defined by the van Genuchten model. In this case, the retention curve may change with the opening of the embedded fractures as pore size controls the gas entry values, and fractures may represent large pores leading to a reduction of the gas entry value. Relative permeabilities are also assumed to be fracture-dependent to account for preferential paths. This is achieved by assuming that the relative permeability, which is a function of the effective degree of saturation, is decomposed into matrix and fracture terms, as discussed in the following paragraph.
- **Constitutive relations for the mechanical behaviour**: deformation is modelled assuming elasticity with net stress (fluid pressure as the maximum between gas and liquid). A dilatancy term (ψ angle) is added in the deviatoric component of the volumetric strains

$$\Delta\varepsilon_v = \frac{\Delta p'}{K} - \frac{\Delta q}{3G}\tan\psi \tag{13}$$

$$\Delta\varepsilon_d = \frac{\Delta q}{3G} \tag{14}$$

where p' and q correspond to the net mean stress and deviatoric stress invariants, and K and G to the bulk and shear modulus, respectively (compression positive). As done by LBNL, net mean stress is defined as total stress minus Biot's coefficient multiplied by fluid pressure (maximum difference between gas and liquid pressures).

- **Hydro-mechanical coupling**: in the proposed approach, it is assumed that the mechanical constitutive model and the permeability model are coupled but independent. That is, the mechanical behaviour is coupled to the hydraulic/gas pressure because the volumetric strains cause changes in permeability, through changes in aperture.

To account for the preferential paths, a constitutive model based on an integrated embedded permeability is employed. The strategy is based on the decomposition of the intrinsic permeability into a matrix and a fracture intrinsic permeability

$$k_{\text{int}} = k_{\text{matrix}} + k_{\text{fracture}} \tag{15}$$

which undergo respective variation with porosity and aperture and read

$$k_{\text{matrix}} = \frac{k_0(1-\phi_0)^2}{\phi_0^3}\frac{\phi^3}{(1-\phi)^2} \tag{16}$$

$$k_{\text{fracture}} = \frac{b^3}{12a} \tag{17}$$

where k_0 (m^2) is the initial permeability (randomly distributed along the material); ϕ_0 (=0.44) is the initial porosity; ϕ (-) is the current porosity value, changing in space and time during the test; a (m) refers to the associated width for each fracture (which is equivalent to the assumed spacing between fractures) and b (m) is the aperture of the fractures. This value depends on the change in strains and is computed as

$$b = b_0 + \langle\varepsilon - \varepsilon_0\rangle a \le b_{\max} \tag{18}$$

with ε (-) being the strain level,ε_0 (-) being the initial strain, b_0 (m) being the initial aperture of the fractures and $b_{\max}$ (m), being its maximum aperture. Liquid- and gas-phase permeabilities are also decomposed into matrix and discontinuity or fracture terms. These read

$$k_{\text{liquid}} = \left(S_{\text{eff, liquid}}\right)^{n_{\text{liquid}}}\left(k_{\text{matrix}} + k_{\text{fractures}}\right) \tag{19}$$

$$k_{\text{gas}} = \left(S_{\text{eff, gas}}\right)^{n_{\text{gas}}^{\text{matrix}}} k_{\text{matrix}} + \left(S_{\text{eff, gas}}\right)^{n_{\text{gas}}^{\text{fractures}}} k_{\text{fractures}} \tag{20}$$

respectively, with $S_{\text{eff, liquid/gas}}$ (-) being the saturation degree for liquid or gas and $n_{\text{liquid/gas}}^{\text{matrix/fractures}}$ (-) a power for each case state (i.e., for liquid or gas state, and for matrix or fractures media). As previously stated, liquid and gas relative permeabilities are defined by the effective saturation degree of liquid and gas respectively. Hence,

$$k_{\text{r,liquid/gas}} = \left(S_{\text{eff, liquid/gas}}\right)^{n_{\text{liquid/gas}}} = \left(\frac{S_{\text{liquid/gas}} - S_{\text{liquid/gas}}^{\min}}{S_{\text{liquid/gas}}^{\max} - S_{\text{liquid/gas}}^{\min}}\right)^{n_{\text{liquid/gas}}} \tag{21}$$

3.3.1.2. Main conceptual modifications: from the laboratory to the field scale model. As in the case of the previous teams, no conceptual changes were added to the laboratory scale model when simulating the full-scale test. Minor modifications concern the use of interfaces (see Section 3.3.2) and the adjustment of some parameters such as (1) the volume factor of the injection system, (2) the description of the heterogeneity and (3) the sensitivity of Biot's coefficient, with values of 0.5 and 1.0. For a comprehensive discussion of the conceptual model and sensitivity analysis, including detailed results of this study, please see Noghretab et al.[21].

3.3.2. Model geometry and numerical software

Numerical simulations were conducted using the computer software CODE_BRIGHT[23]. CODE_BRIGHT is a simulation program based on the finite element method that has been developed collaboratively by the Universitat Politècnica de Catalunya·BarcelonaTech (DECA-UPC) and the International Centre for Numerical Methods in Engineering (CIMNE).

To simulate the Lasgit experiment, a three-dimensional model has been developed. Initially, a complete model setup was generated, but only a quarter of the model was finally employed for the hydro-gas calculations and calibrations, Fig. 10. The finite element mesh consists of 66948 elements, comprising 62794 tetrahedra for the volumes and 4154 triangles for the surfaces. The mesh encompasses a total of 13170 nodes, resulting in 26340 degrees of freedom. The model's geometry encompasses various components, including the coping (consisting of a concrete plug and steel lid), the canister (comprising inner and outer copper walls), bentonite rings and cylinders, pellets and rock (Fig. 11) to depict the entire system's dimensions accurately.

At the injection section, the mesh has been generated with 4538 elements (4380 tetrahedra for the volumes and 158 triangles for surfaces), with a total of 1078 nodes. The model geometry dimensions, including the canister, bentonite rings cylinders, pellets, and filter arrays, have been made in agreement with the test specifications provided by the British Geological Survey (Fig. 11).

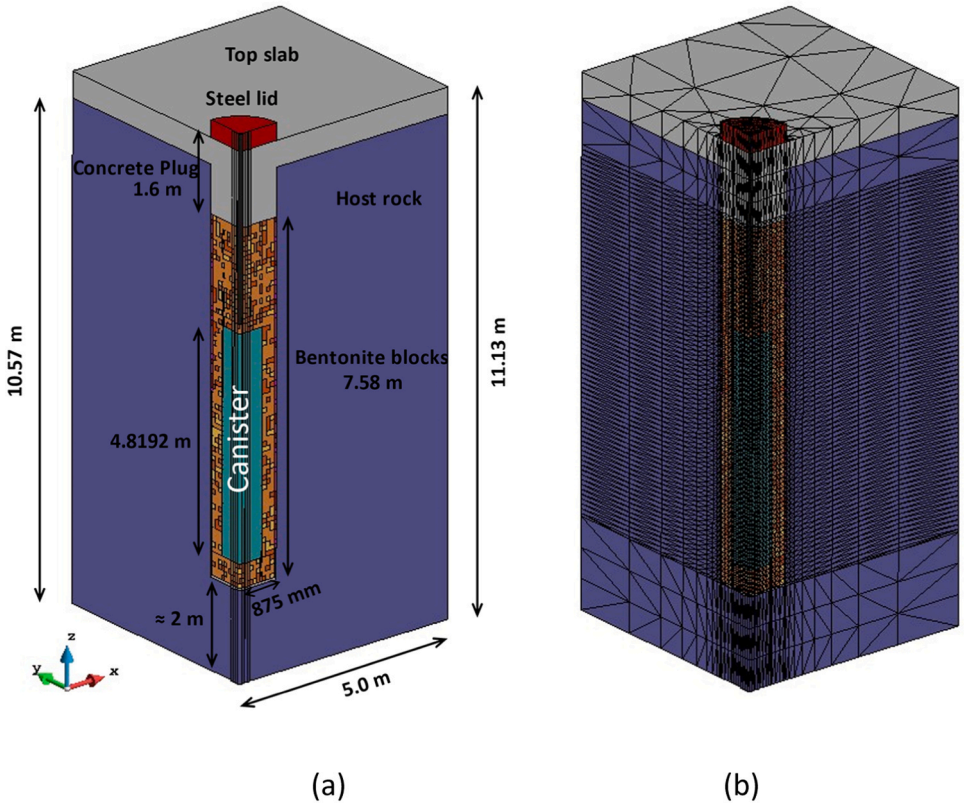

Fig. 10. The ¼ model geometry used by CIMNE-UPC/Andra to simulate the full-scale test: (a) shows a general view of the model and (b) shows the mesh (with 66948 tetrahedra and triangle elements with 13170 total nodes), from Noghretab et al.[21].

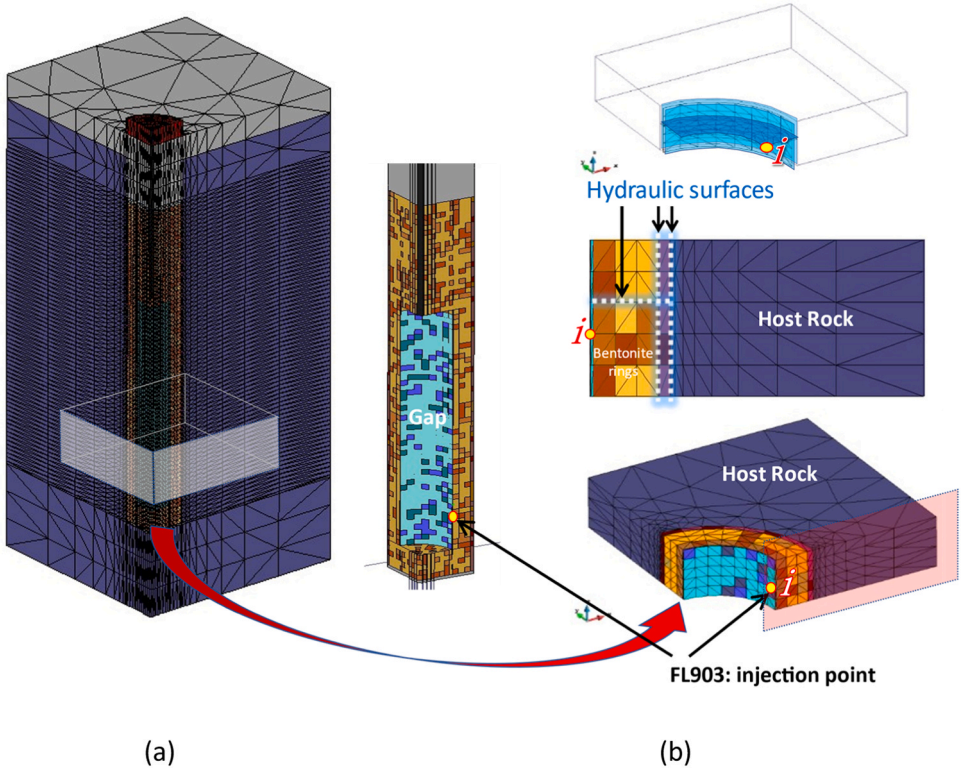

Fig. 11. Model geometry and 3D FE models for (a) the 1/4 full-setup and (b) the injection section model (from[21]).

The model includes additional hydraulic surfaces, which have been modelled at the bentonite block contacts (i.e., horizontal interface surfaces) and at the bentonite/pellets and pellets/rock contacts (i.e., vertical interface surfaces), as shown in Fig. 12. Although these interfaces exhibited similar properties to the bentonite material, they have been considered as separate materials with distinct permeabilities to potentially serve as pathways for gas migration through the buffer. A sensitivity analysis on hydraulic transmissivity was conducted by varying the intrinsic permeability values in both horizontal and vertical directions to assess their impact on system behavior. Four cases were considered: horizontal sensitivity, vertical sensitivity, combined horizontal and vertical sensitivity, and a base case, with permeability values ranging from 1.0×10^{-17} m² to 1.0×10^{-20} m² (for more detail please see[21]).

Filter arrays have also been included, represented by external surfaces with a thickness of 1 mm, complemented by a triangular mesh (Fig. 13). Flow rates and pressures have been prescribed at the outer nodes of these surfaces, and each surface has been connected to a single node located on the outer surface of the canister's copper wall, specifically at the Filter Array position. These external surfaces (see Fig. 13) have proven to effectively capture the system volumes associated with pipework, the injection vessel pump, and any additional devices present in the gas injection system before the gas enters the sample. The representation of these components in the model has been achieved through the application of an equivalent injection volume factor (a calibrated parameter) to these injection filter surfaces, as similarly done in other approaches (e.g., LBNL model).

A heterogeneous medium has been considered for the full-scale test (Fig. 14). In this study, the geometrical domain of the bentonite (rings and cylinders), pellets and gap (that is expected to be filled by the surrounding bentonite after swelling) has been divided into small sub-zones to which different initial properties have been assigned, as seen in Fig. 14. In particular, three different permeability distributions have been assumed. They follow a probabilistic model, incorporating a layer-by-layer random permeability distribution in three different zones. As a base case scenario, the permeabilities in these zones have been arbitrarily weighted with 2/3, 1/6, and 1/6 with values of 1×10^{-21} m^2, 1×10^{-20} m^2, and 1×10^{-19} m^2 respectively. A sensitivity analysis has also been performed to better understand the impact of the different proportions of the heterogeneity distribution on the calculated gas pressure. From a practical point of view, the impact of this sensitivity on the calculated results was found to be small.

In the gap layer, intrinsic permeability values varied according to three different states of the gap closure (Fig. 15), see Table 3. It is important to note that changes in porosity do not affect the model's predictive capability. Thus, for simplicity, a constant porosity has been assumed for the bentonite and pellet materials. Results are presented in Noghretab et al.[21].

3.3.3. Initial and boundary conditions

The system is initially assumed to be water-saturated with a constant pore pressure of 0.1 MPa (atmospheric pressure has been assumed). Furthermore, the gas pressure and liquid pressure at the external surfaces, which simulate the injected gas volume, are set equal to 0.1 MPa. The initial stress conditions at the rock are considered as 10.5 MPa in the horizontal directions (x and y) and 5.25 MPa in the vertical direction. The initial stresses on the bentonite cylinders are both (axial and radial) considered as −6 MPa. The boundary conditions have been carefully selected to align with the specified Lasgit set-up, specifically through the use of the Filter array FL903. These assumptions and boundary conditions are crucial in accurately capturing the behaviour of the gas test and ensuring the model's alignment with the experimental setup.

3.4. Model developed by KAERI

3.4.1. Conceptual model

This model is built on the work carried out by KAERI within the previous phase of the DECOVALEX project, see Lee et al. (2019, 2020), in which the team developed a hydro-mechanical model for the migration of gas through a low-permeable material that included a damage model to account for the deterioration of the rock after gas breakthrough. Indeed, for the current phase of DECOVALEX-2023, KAERI developed a hydro-mechanical model based on standard multi-phase flow theory, whose key features are:

- **Constitutive relations for the hydraulic and gas behaviour**: the classical multi-phase Darcy law is solved with a mass balance equation for each component (water and gas phases), assuming constant temperature.
- **Constitutive relations for the mechanical behaviour**: the classical two-phase flow model is coupled to an elastic damage model proposed by Tang et al.[38]. According to this model, the host rock is assumed to be brittle-elastic. That is, the stress-strain relationship is divided into an elastic phase (where no damage or irreversible damages occur) and a damage phase, that accounts for the

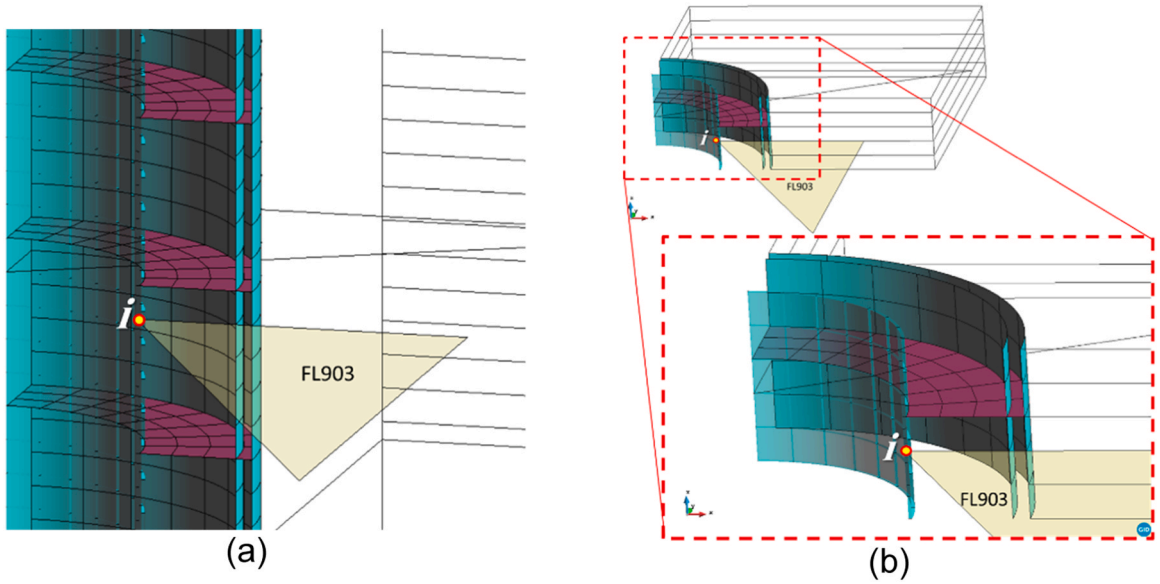

Fig. 12. Model geometry of horizontal and vertical interfaces and their position to the injection point (FL903): (a) 1/4 full set-up, (b) injection section model.

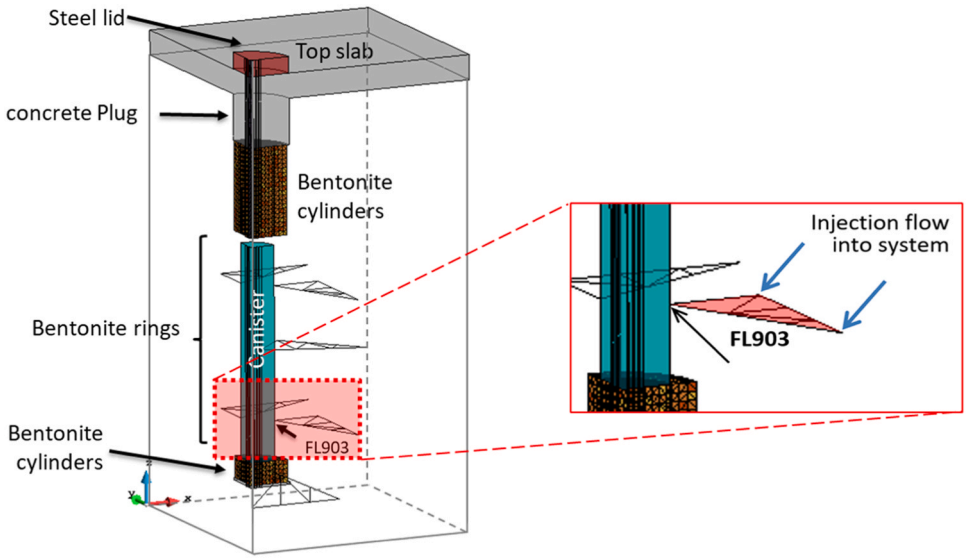

Fig. 13. Injection filter details (FL903 filter array location): external volumes to prescribe given injection gas volume-into-system flow rates (external volume equivalent to the system volume). An initial total injector volume of 2.0 cm^3 has been prescribed (from[21]).

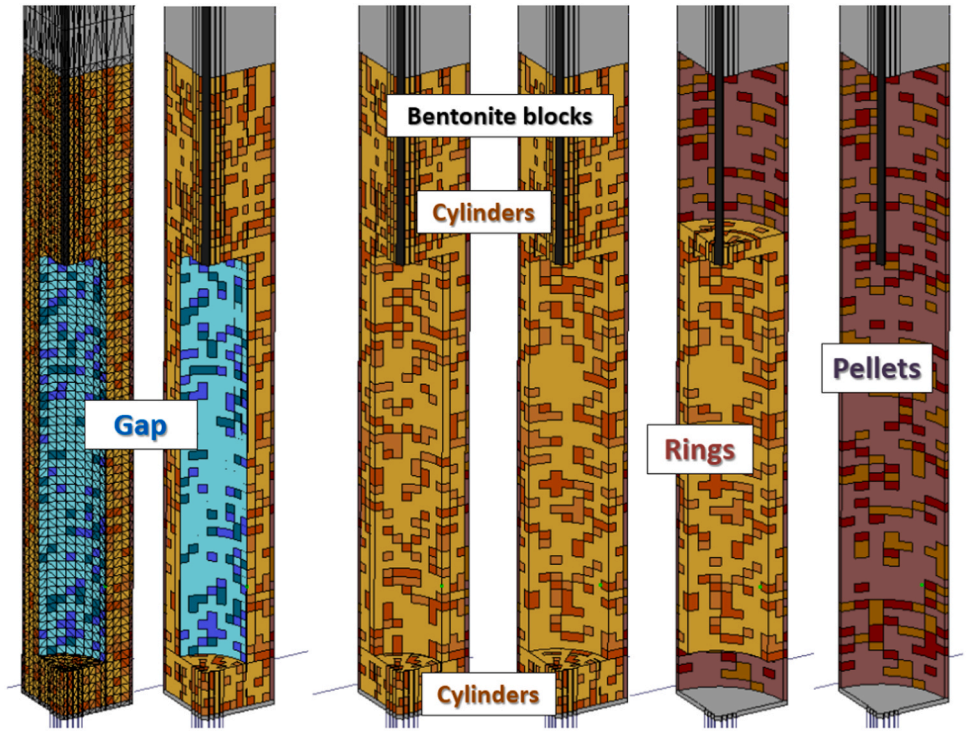

Fig. 14. Heterogeneity on permeability randomly distributed to the bentonite blocks (cylinders and rings), pellets, and gap (1/4 full-setup) (from[21]).

deterioration of the rock (decrease of strength, rigidity and toughness, for instance). The effective stress tensor $\boldsymbol{\sigma}'$ (Pa) is thus defined as

$$\begin{aligned} &\text{Before gas breakthrough (elastic model)}: \quad \boldsymbol{\sigma}' = \mathbf{C} : \boldsymbol{\varepsilon} \\ &\text{After gas breakthrough (damage model)}: \boldsymbol{\sigma}' = (1-D)\mathbf{C} : \boldsymbol{\varepsilon} \end{aligned} \tag{22}$$

where $\boldsymbol{\varepsilon}$ (-) is the infinitesimal strain tensor, $\mathbf{C}$ (Pa) is the fourth-order stiffness tensor, D (-) is the damage parameter and: is the double tensor contraction.

As seen in Eq. 22, the elastic modulus of the rock progressively degrades as damage grows. In fact, only damage under tensile stress was considered and hence, damage induced by the compressive stress was not included into the model. Hence, when the tensile stress in an element reaches its tensile strength, the damage variable

$$D = \begin{cases} 0 & \varepsilon \leq \varepsilon_{t_o} \\ 1 - \dfrac{f_{tr}}{E_0 \varepsilon} & \varepsilon_{t_o} \leq \varepsilon \leq \varepsilon_{t_u} \\ 1 & \varepsilon_{t_u} \leq \varepsilon \end{cases} \tag{23}$$

is used, where f_{tr} (Pa) stands for the residual tensile strength, E_0 (Pa) is the initial (or undamaged) elastic modulus, ε (-) is the principal

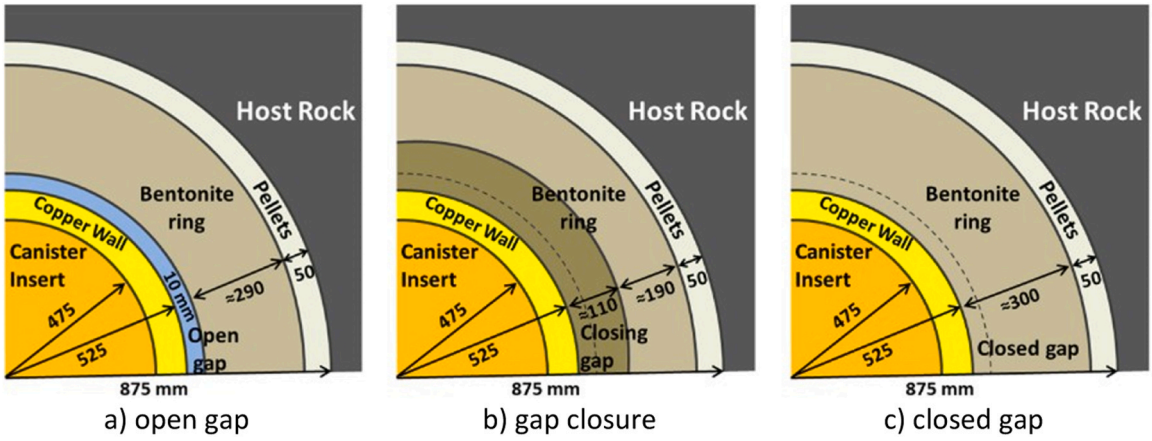

Fig. 15. Model geometry: gap closure scenarios: (a) open gap/initial state, (b) transitional gap-closure, and (c) closed gap/homogenized states. (Measurements in mm, from[21]).

Table 3
Heterogeneity on permeability random distribution.

Materials	Distribution (weighting) strategy	Intrinsic permeability	Porosity
Bentonite	1/6 = 16.7 %	1.0×10^{-19} m^2$1.0\times10^{-20}$	0.366
Pellets	1/6 = 16.7 %	m^2$1.0\times10^{-21}$ m^2	0.706
	2/3 = 66.7 %		
Gap	1/6 = 16.7 %	Variable Intrinsic permeability and	
	1/6 = 16.7 %	porosity(According to Gap closure states:	
	2/3 = 66.7 %	open – transitional – closed scenarios)	

strain and ε_{t_o} (-), ε_{t_u} (-) are tensile strain limits.

- **Hydro-mechanical coupling**: standard Biot's theory is assumed to describe the hydro-mechanical coupling with

$$\boldsymbol{\sigma}' = \boldsymbol{\sigma} - \alpha\bar{p}\mathbf{I} \tag{24}$$

and

$$\bar{p} = S_g p_g + S_w p_w \tag{25}$$

This is used to define the linear momentum balance equation of the porous medium

$$\nabla(\boldsymbol{\sigma} - \alpha\bar{p}\mathbf{I}) + \rho\boldsymbol{g} = 0 \tag{26}$$

Dilatant pathways are modelled by including a damaged-dependent intrinsic permeability field, where

$$k_{int} = k_{int,undamaged} + k_{int,damaged} \tag{27}$$

and

$$k_{int,undamaged} = k_{int,0} e^{A\left(\frac{\phi}{\phi_0}-1\right)} \tag{28}$$

$$k_{int,damaged} = \frac{D}{D_{kmax}}\left(k_{max} - k_{int,undamaged}\right) \tag{29}$$

being $k_{int,0}$ (m^2) the initial intrinsic permeability, A (-) an empirical factor calibrated from the experimental tests, k_{max} (m^2) the experimental maximum permeability of the damaged bentonite and D_{kmax} (-) the experimental rock damage value that corresponds to k_{max}.

The two main modifications with respect to the approach employed in the DECOVALEX-2019 phase are (1) the inclusion of the interface between the void and the buffer material and (2) the designation of different material properties for each of the different elements that compose the domain under consideration (e.g., void, bentonite, pellets and rock).

3.4.2. Model geometry and numerical software

To simulate the full-scale model, the COMSOL Multiphysics® (see[4]) software was used. Consistent with BGR/UFZ and CIMNE-UPC/Andra, only one quarter of the bentonite cylinder was considered, Fig. 16.

3.4.3. Initial and boundary conditions

The initial gas pressure was prescribed at 1868 kPa, and the initial water saturation was 0.99. The capillary pressure was calculated using the van Genuchten model and then, the initial water pressure was calculated from the initial gas pressure and capillary pressure. Regarding the mechanical model, the initial total stress tensor was assumed to be diagonal with $\sigma_{xx} = \sigma_{xx} = -5$ MPa and $\sigma_{zz} = -6$ MPa, where the sign minus means compression. Temperature is supposed to be prescribed at 20 °C.

The initial gas pressure was assigned to the outer boundary of the rock components and the injection pressure data over time was applied to the injection area as a Dirichlet boundary condition. Regarding the mechanical model, a fixed constraint boundary was applied to the bottom surface, and a roller boundary was applied to all boundaries except at the bottom surface.

4. Results

The capabilities of four numerical models (BGR/UFZ, LBNL, CIMNE-UPC/Andra and KAERI) were assessed by comparing the simulated results against the experimental data obtained from the Lasgit experiment performed at the Äspö Hard Rock Laboratory. Teams were asked to provide scientific evidence that the developed models are able to capture the main key aspects of the experimental time series data rather than the exact details of the test stage. This is due to the fact that, as already seen when modelling laboratory-scale experiments (see[36]), experimental data exhibits a combination of deterministic and stochastic behaviours and thus, models need to account only for the key experimental features reproducible across all experiments.

In particular, teams were asked to prove that their models are able to capture the following seven features:

1. As gas is being injected into the system (**evolution of the injection pressure**), a
2. **rapid gas breakthrough** is observed.
3. This occurs at a **particular breakthrough time** and at a
4. **very low gas saturation**, which then leads to a
5. **gas peak value**, which is then followed by a
6. **decay** to steady state (and subsequent decays as inflow rate is reduced).

These key features are observed together with

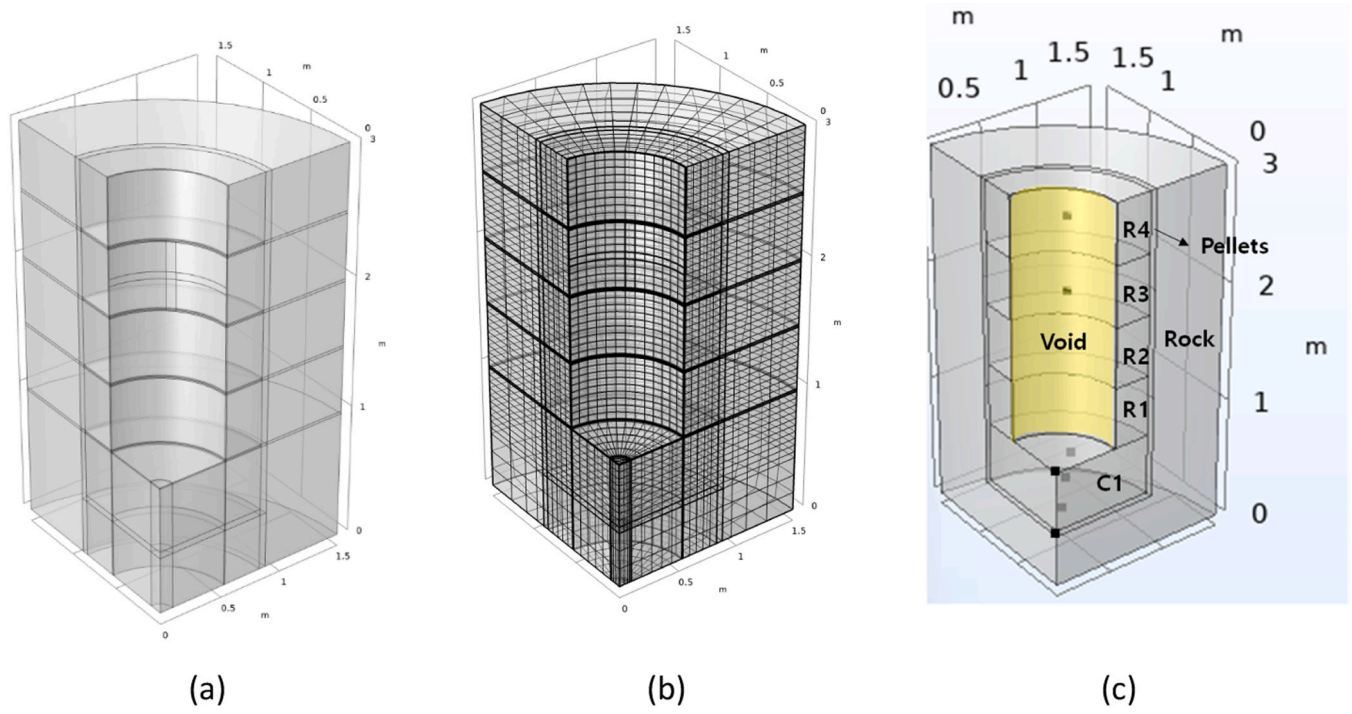

Fig. 16. As done by other teams, [a] only a quarter of the bentonite cylinder was considered. [b] A mesh with 9635 elements (hexahedral and tetrahedral for the cylindrical shapes) and 11067 nodes was used by KAERI, with [c] showing the different materials considered in the model. As described above, KAERI's model applied gas injection as a Dirichlet boundary condition using existing experimental data. Therefore, the injector volume was not modeled separately, although the Dirichlet boundary area for gas injection simulation is about 0.03 m^2.

7. **small variations in pore pressures and stresses.**

Here, for the sake of comparison, final numerical outcomes (obtained after different sensitivity analyses) are employed. For a detailed overview of the development process and the sensitivity analysis performed within the DECOVALEX-2023 phase, we refer to the individual contributions of the modelling participants (see for instance contributions by[25] and[21]).

In order to assess key features 1, 2, 3, 5 and 6, the evolution of the injection pressure is shown in Fig. 17. As observed, only three models can actually be assessed, as the KAERI model uses the injection pressure as input data (Dirichlet boundary condition). As seen, the three numerical approaches are able to predict the overall experimental response during the first three gas ramps. However,

- At day 3163.04, when the fourth and final pressure ramp was started, differences are observed in the response predicted by the model developed by CIMNE-UPC/Andra. Indeed, a slower pressurisation response is observed as compared to the experimental behaviour, leading to a later gas peak pressure (at day 3250, that is 44 days later than in the field). This relates to the way in which gas pressure is coupled to gas permeability within the model. This coupling also results in inflow of gas from the beginning of the test (see Fig. 18). The gas peak pressure value is well predicted (with less than a 2 % error) and the characteristic decay of pressure is also well captured.
- At day 3197.9, an initial gas peak pressure of 5.92 MPa is predicted by the BGR/UFZ model indicating that a first small gas entry occurs. The cause for this initial peak pressure is unclear, but after it, the model predicts a rapid response. This is followed by a second pressurisation phase leading to a peak gas pressure of 6.01 MPa (less than a 3 % error with respect to the experimental value) at day 3205.5.

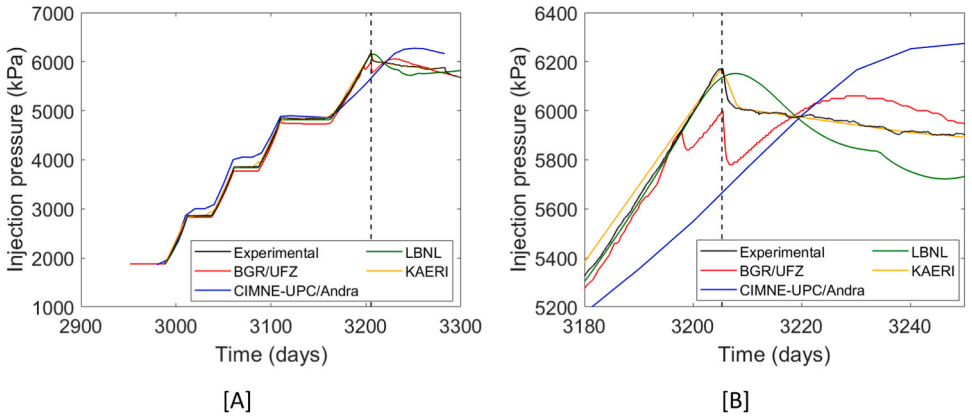

Fig. 17. The filter pressure of FL903 during Gas Injection Test 4. [A] Evolution of both the experimental and numerical outputs and [B] detail around the peak pressure time. Black dashed line in this figure and in subsequent figures indicates peak pressure.

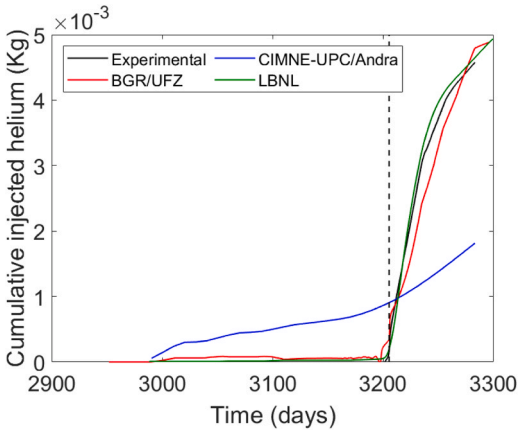

Fig. 18. Cumulative injection mass predicted by different teams. As KAERI model uses the injection pressure as input data (Dirichlet boundary condition), it has not been shown here.

Following breakthrough, inflow to the clay spontaneously decreases until day 3207, when gas pressure begins to slowly increase. During this time gas flow into the bentonite continued at a slower rate, Fig. 18, while gas pressure slowly increased, peaking at 6.06 MPa at day 3228.18 (i.e., 28 days later than in the field). Thereafter gas pressure exhibited the characteristic negative pressure transient closely matching the data.

- The LBNL model can correctly capture the evolution of the injection pressure. Indeed, a gas peak pressure of 6.15 MPa (with less than a 0.4 % error with respect to the experimental value) is captured at day 3207.7 (only two days later than experimental response). However, around day 3246, the post-peak gas pressure shows a positive trend in contrast to the data which shows a sharp decay in pressure after its peak. A smother pressure and flow response in the LBNL model might be related to averaging fluid storage over continuum elements compared to the pore-volume available for gas flow dilatant channels.(Fig. 19)

The fourth key feature (very low gas saturation) is assessed by means

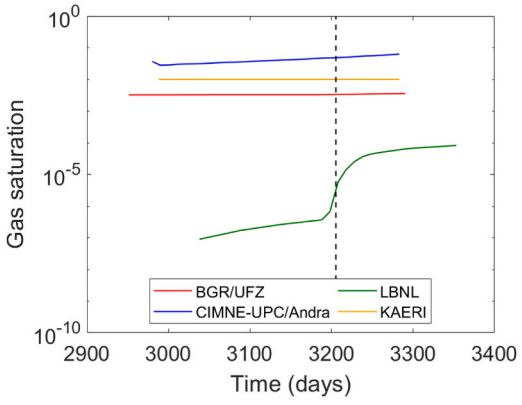

Fig. 19. Average gas saturation profiles (y-axis in logarithmic scale). Note that a straight comparison is not easy, as average values depend on the density of the mesh within each model and the technique for averaging that each team has used.

of different outputs. First, the average gas saturation profile is analysed.[1] As seen from the gas saturation time-series data (Fig. 20), all models capture gas flow with very low gas saturation. The BGR/UFZ and KAERI models predict small changes in saturation (a difference of 3.4 $\times 10^{-4}$ was observed between maximum and minimum for the BGR/UFZ model, and a difference of 1.2 $\times 10^{-3}$ was observed for the KAERI model). Gas saturation values at three different timings (at initial time of the simulation, at the time where the model predicts the gas pressure peak and at final day 3283) and at three different distances from the centre of the canister (at 575 mm, at 725 mm and at 850 mm) at the level of the injection filter, see the scheme in Fig. 20, are shown in Table 4. As reported, saturation values lie between 0 and 0.127. In particular, gas saturation predicted by BGR/UFZ far away from the centre of the canister (i.e., at 725 and 850 mm) is constant during all the simulation (i.e. 0.003) whereas small variations of gas saturation (from 0.001 to 0.004) are predicted near the centre of the canister (at 575 mm). A similar behaviour is observed by LBNL's model, as gas saturation far away from the centre of the canister vanishes during all the simulation whereas gas saturation at 575 mm from the centre of the canister reaches a final value of 0.054. KAERI's model predict tiny variations during all the simulation everywhere, as gas saturation values lie between 0.010 and 0.014. CIMNE-UPC/Andra also captures small gas variations away from the canister (from 0.002 to 0.090). However, higher gas saturation values are predicted near the centre of the canister once the breakthrough is reached (around 0.12). In general, all models predict that gas flow is very localised within the swollen bentonite and the bentonite interfaces, as expected, see Fig. 21. However, in the conceptual model of dilatant gas flow, gas saturation at specific points within the model should be either zero or 100 % (i.e., outside or inside a dilatant gas pathway respectively). Thus, the presence of low gas saturations likely reflects the averaging of saturation values across the plane of reference, which could be either a 2D surface or a 3D volume. It is also likely to stem from the mismatch in physics between the conceptual model of dilatant pathway creation and the continuous models used by the teams. In the latter, all models link gas pressure to permeability which, through retention functions, result in the displacement of water and gas penetration of the surrounding clay. However, this mode of desaturation was not observed in the post mortem data from Lasgit[7] or in the laboratory data used in previous phases of the project[35,36], all of which resulted in post-test water saturations of ~100 %.

To assess the seventh key feature, a visual inspection of the stress and pore pressure data is required. As shown in Fig. 22A, all the models but KAERI are able to predict radial stresses within the experimental bounds. While BGR/UFZ, LBNL and KAERI models can simulate the experimentally-observed small variations, see Fig. 22B, CIMNE-UPC/Andra values present higher variations. In particular, CIMNE-UPC/Andra's stress values present a piecewise-linear function with a clear turning point at day 3250 (when breakthrough is predicted by their model). This is due to the fact that, as radial stress responds to pore pressure and effective stress cannot change significantly due to the absence of total volume changes, pore pressure and total stress change jointly. As shown in Fig. 22C, average numerical pore pressures obtained with different models present significant differences. BGR/UFZ and LBNL are able to capture very small variations in terms of pore pressures (in Fig. 22C, some model results seem constant due to the scale). However, BGR/UFZ results are higher than expected and do not lie within the experimental bounds. CIME-UPC/Andra outputs are characterised by small variations until the experimental breakthrough occurs. Beyond this point, the model predicts an increment of pressures reaching a maximum value at day 3280. Finally, as KAERI's pore pressure is fully coupled to the injection pressure a direct correlation is observed (see

[1] A mass balance between inflow and outflow could have been conducted to calculate saturation profiles; however, the teams were not required to provide this data during the study.

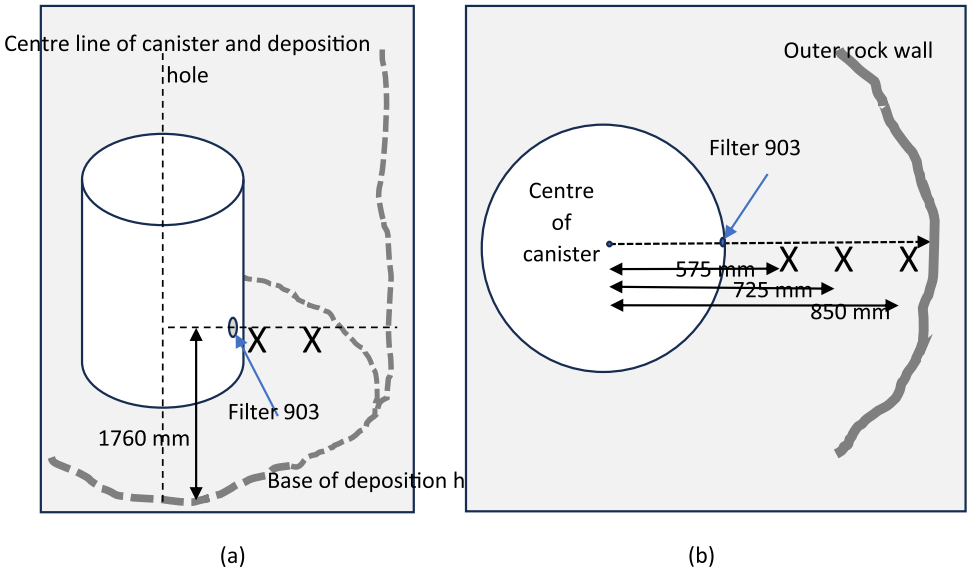

Fig. 20. Schematic drawing of the locations where gas saturation is being assessed: (a) side and (b) plan views.

Table 4
Gas saturation values predicted by the teams at different locations and at different timings.

		Initial time	Time where gas peak is reached	At day 3283
At 575 mm from the centre of the canister	BGR/UF	0.001	0.004	0.004
	LBNL	0.000	0.042	0.054
	CIMNE-UPC/Andra	0.019	0.115	0.127
	KAERI	0.010	0.014	0.013
At 725 mm from the centre of the canister	BGR/UF	0.003	0.003	0.003
	LBNL	0.000	0.000	0.000
	CIMNE-UPC/Andra	0.002	0.012	0.019
	KAERI	0.010	0.014	0.014
At 850 mm from the centre of the canister	BGR/UF	0.003	0.003	0.003
	LBNL	0.000	0.000	0.000
	CIMNE-UPC/Andra	0.090	0.088	0.087
	KAERI	0.010	0.012	0.012

Fig. 22). As such, the experimentally-observed small variations are not reproduced and hence, the complexity of the process is not fully described.

5. Discussion

This paper presents a summary of work performed in Task B of the current phase of DECOVALEX (DECOVALEX-2023) in which four teams have developed hydro-mechanical approaches for the modelling and representation of dilatant-controlled advective gas flow through very low-permeability materials. This study has allowed teams (BGR/UFZ, LBNL, CIMNE-UPC/Andra and KAERI) to test their enriched multi-phase flow models and codes and enhance them in order to include the main deterministic features observed in a field scale gas injection test.

BGR/UFZ employed a fully coupled hydro-mechanical approach which combined two-phase flow with an elasto-plastic model. To generate dilatancy-induced areas, this approach combined an empirical strain-dependent permeability approach with a dual heterogeneous distribution of Young's modulus and gas entry pressure. The model is able to predict the experimentally-observed rapid response. It captures a first small gas entry, possibly triggered by a lower value of the gas entry pressure or Young's modulus near the injector, which enabled the release of some gas into parts of the bentonite. However, due to the applied inhomogeneity, the affected area might be spatially limited. After that, the model predicts the peak gas pressure with less than a 3 % error with respect to the experimental value. Following breakthrough, the decay in inflow is correctly modelled until day 3207, when gas pressure slowly increases peaking at 6.06 MPa at day 3228.18 (i.e., 28 days later than in the field). It is assumed that this behaviour is due to the following correlation: The gas inflow into the injector continues, but the gas pressure is reduced to a small extent due to the increased gas outflow in the vicinity of the injector and the increased available gaseous pore-space. As a result, the increase in permeability in the bentonite and the local displacement of the water is reduced for a short time. This behaviour is caused by the relation between deformation and permeability, but cannot fully reproduce the typical dilatancy-controlled gas flow in bentonite in which often one major gas breakthrough is observed.

LBNL used a sequentially coupled approach that assumed clay behaves as a linear elastic medium (with swelling stress) and that permeability depends on the gas pressure and the effective minimum compressive stress. To allow localisation of gas flow, this model assumed a fracture-like behaviour of the flow path. This model is able to correctly capture the evolution of the injection pressure. Indeed, a gas peak pressure of 6.15 MPa (with less than a 0.4 % error with respect to the experimental value) is captured at day 3207.7 (only two days later than experimental response). However, around day 3246, the post-peak gas pressure also shows a positive trend in contrast to the data. In general, the LBNL model shows a smother response in gas flow and pressure around the peak pressure compared to that of the experiments, both for the laboratory and field experiments. This might be related to averaging fluid storage over continuum elements compared to the pore-volume available for gas flow dilatant channels. A potential remedy could be to consider dual-porosity medium and/or model parameters of more rapid changes in permeability when gas pressure reaches confining stress.

CIMNE-UPC/Andra developed a coupled hydro-mechanical model assuming a heterogeneous initial permeability field with embedded fractures. To account for the development of preferential paths, a constitutive model based on an integrated embedded permeability was employed. In this model dilatant pathways were modelled by decomposing the intrinsic permeability into a matrix and a fracture intrinsic permeability. The model predicts a slower pressurisation response as compared to the experimental behaviour, leading to a later gas peak pressure (at day 3250, that is 44 days later than in the field). This relates

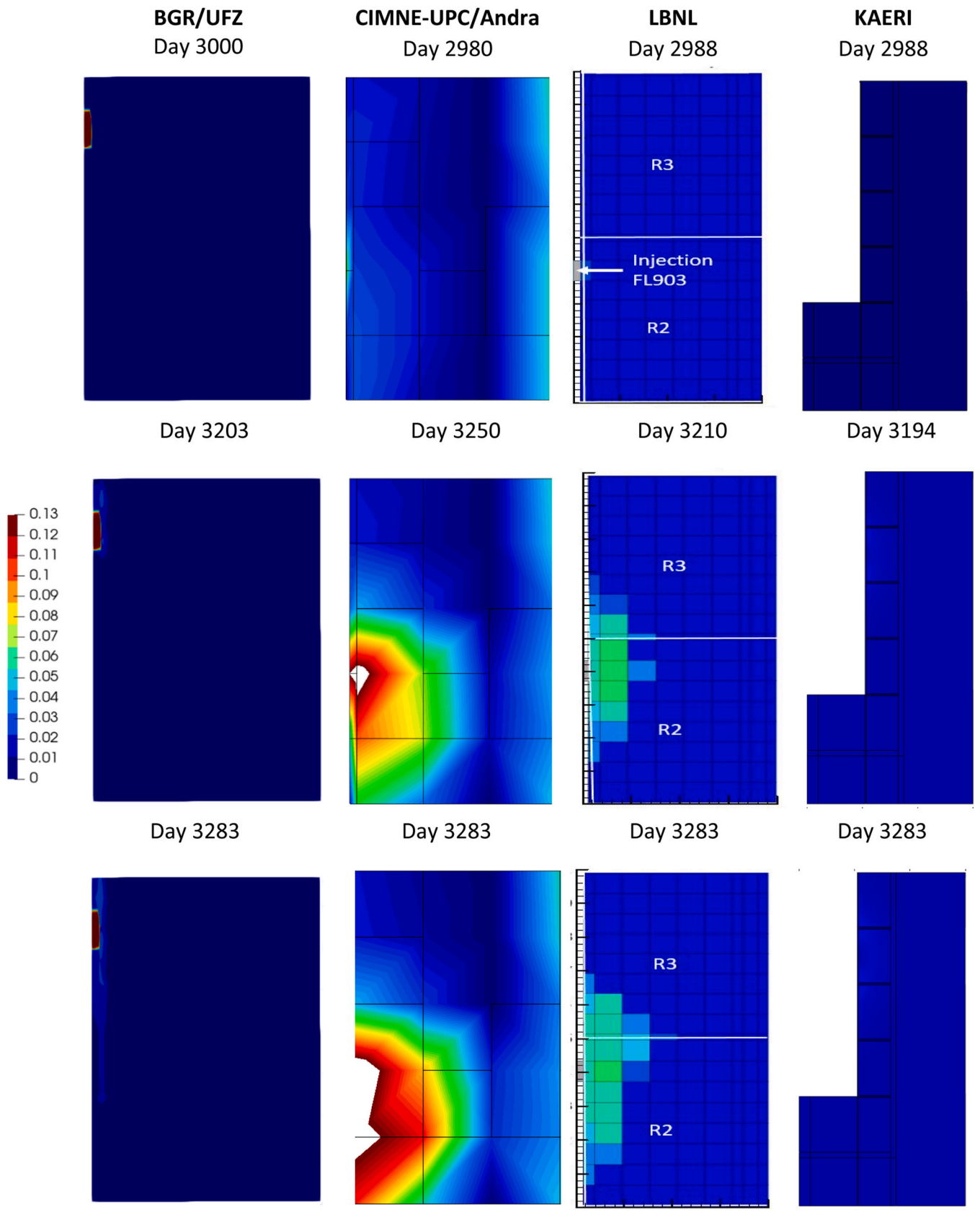

Fig. 21. Average gas saturation contour plots (across a two-dimensional surface tangential to filter FL903) predicted by the teams (BGR/UFZ in column 1, CIMNE-UPC/Andra in column 2, LBNL in column 3 and KAERI in column 4). Each row corresponds to a different time of the simulation (at initial time of the simulation, at the time where the model predicts the gas pressure peak and at day 3283).

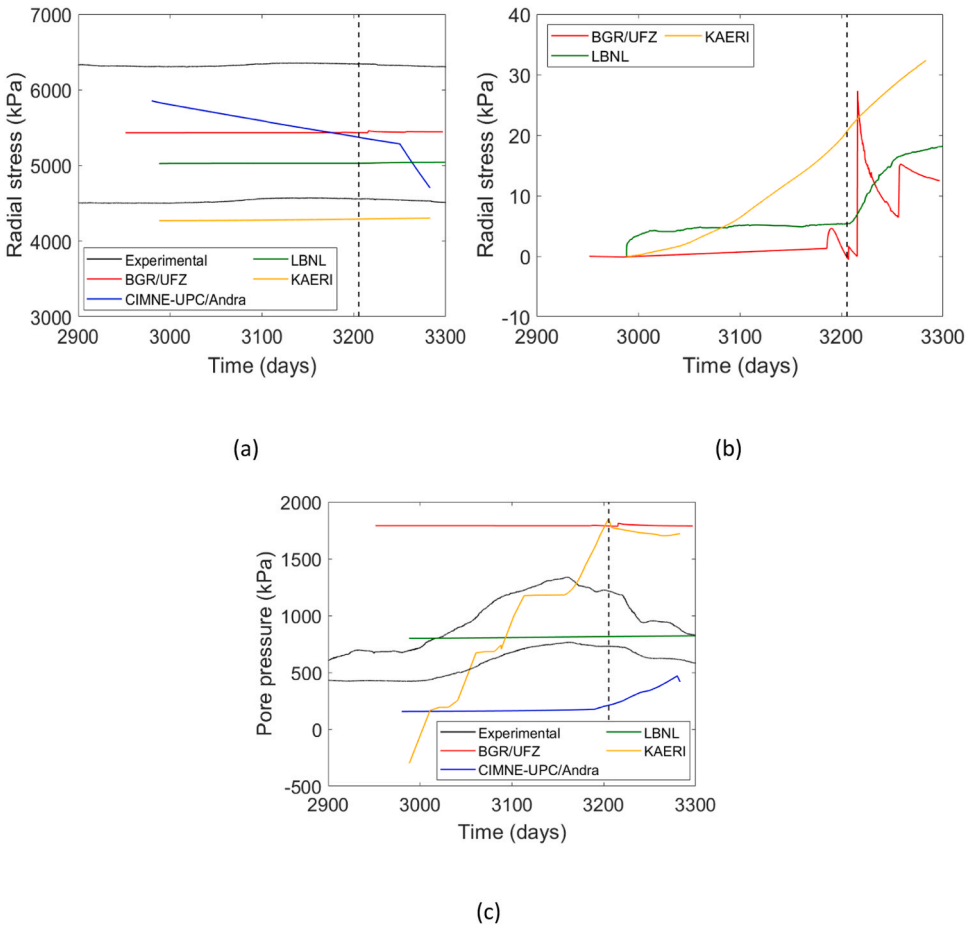

Fig. 22. Average (a) radial stresses and (c) pore pressures obtained with the four numerical models plotted against the maximum and minimum experimentally-obtained values. (b) shows normalised radial stresses (note that UPC results have not been included since variations can already be seen in (a).

to the way in which gas pressure is coupled to gas permeability within the model. However, the gas peak pressure value is well predicted (with less than a 2 % error) and the characteristic decay of pressure is also well captured.

KAERI developed a hydro-mechanical model based on standard multi-phase flow theory and an elastic damage model. Dilatant pathways are modelled by including (1) a damaged-dependent intrinsic permeability field, (2) interfaces between the void and the buffer material and (3) different material properties for each of the different elements that compose the domain under consideration. Although the model cannot be assessed using most of the validation features (as it uses the injection pressure as input data), the model is found to correctly capture the experimentally-observed small variations, although radial stresses do not lie within the experimental bounds.

In summary, this study illustrates that the models used, which were originally developed and calibrated against laboratory scale tests, did not need substantial modification to simulate the full-scale experiment. Indeed, model parameters calibrated and validated at laboratory-scale have been applied to predict field-scale gas flow at Lasgit, including peak gas pressure and injected cumulative gas volume. The only exception was the introduction of interfaces between blocks to reflect the experimental configuration. Inclusion of these features within the codes necessitated changing of some parameters (e.g., assuming higher permeability). These adjusted models were then able to represent most of the key features observed in the experimental data. Small differences between the model predictions and the experimental data, such as the timing and stress changes during the transitional phase during gas entry, the evolution in gas flow following breakthrough or the post peak negative transient phase, all stem from the fundamental differences between the modelling approaches (based on the physics of visco capillary flow) and that of the data (based on dilatant pathway flow). However, there are still some numerical features (e.g., positive trends in pressure, earlier/later peak pressure predictions) that are not fully represented, since the discrepancy between the physics of the models and that of the process governing gas flow remains a significant challenge.

6. Conclusions

Four different numerical representations for the quantitative description of advective gas flow in clay-based repository systems have been developed and applied to a unique dataset from a large-scale gas injection test (Lasgit) performed at the Äspö Hard Rock Laboratory (Sweden) working towards development and validation of different numerical approaches.

Task B within DECOVALEX-2023 has explored the refinement of these numerical strategies applied to the simulation of gas flow at a field scale. In particular:

1. BGR/UFZ approach combines a two-phase flow with an elasto-plastic model, which was able to predict the experimentally-observed rapid response. This model exemplifies how spatial variability of individual material properties can influence gas pressure development in a large model: indeed, spatial heterogeneities play a less significant role than interfaces and continuum-scale inhomogeneity based on different incorporated materials.
2. LBNL's approach is a continuum model with the key feature that permeability is directly related to the least compressive effective

stress. Thus, permeability changes caused by other processes such as elasto-plastic shear damage could not be captured. The model applied in this study is able to correctly capture the timing of gas breakthrough, the peak pressure at gas breakthrough as well as the cumulative gas flow was well captured. However, it tends to produce a smother continuum response not capturing sharp spikes in gas flow rates at gas entry. This indicates that the sharp short spikes in gas flow rate involve a relatively small gas volume that have a small impact on the cumulative gas flow entering the system.

3. UPC's model performs gas injection into a system defined by material heterogeneity and hydraulic interfaces between blocks and system components (bentonite-pellets-rock). Gap closure assumptions were incorporated by introducing three materials for a certain thickness of the bentonite, providing insights into various mechanical gap closure scenarios due to bentonite swelling for the hydraulic model approach. The model demonstrated that embedded fractures and dilatancy significantly influence gas pathways, affecting fracture aperture and entry gas pressure. The model presented in this study approached the maximum gas pressure despite predicting a smoother gas breakthrough response which was delayed when compared to the actual data. Parameter tweaking, such as the volume factor of the injection, was necessary to reflect real-world impacts of gas injection volumes and ensure system sustainability. Future model developments could incorporate constitutive laws for double porosity structures, viscoelasticity, and temperature coupling for THM modeling in case of heating canister tests.
4. KAERI's model combines classical two-phase flow modelling techniques and an elastic behaviour-based damage model and can simulate the formation of a preferential pathway due to breakthrough and the resulting rapid gas movement. Introduction of voids and interfaces between components allowed the correct capture of breakthrough timing. However, the model could not reproduce gas saturation changes, as gas pressure and saturation are considered primary variables. To overcome this limitation, the model could be modified to allow variable gas and water pressures. In addition, the model could be modified so that gas injection could be simulated using the source term.

Work performed within the task reveals that codes do not need to be substantially modified to reproduce full-scale tests: models developed and validated against laboratory scale tests have been slightly modified with the introduction of interfaces between bentonite blocks and by means of (1) the introduction of interfaces between blocks to reflect the experimental configuration and the (2) adjustment of some parameters (e.g., higher permeability). As seen, the updated models are able to represent most of the key features observed in the experimental data, even at a large scale. However, it is noteworthy that the need for an initial calibration of the models against laboratory or field data may limit their use in a predictive manner. Indeed, the complexity of the physical processes combined with a need for detailed calibration, currently limit their use in the quantitative prediction of gas flow. In such circumstance, models should be used with caution. Additional quantitative data, in which the processes governing gas flow are suitably quantified, is required to support continued model development.

Declaration of Competing Interest

The authors declare that they have no known competing financial interests or personal relationships that could have appeared to influence the work reported in this paper.

Acknowledgements

DECOVALEX is an international research project comprising participants from industry, government and academia, focusing on development of understanding, models and codes in complex coupled problems in sub-surface geological and engineering applications; DECOVALEX-2023 is the current phase of the project. The authors appreciate and thank the DECOVALEX-2023 Funding Organisations Andra, BASE, BGE, BGR, CAS, CNSC, COVRA, US DOE, ENRESA, ENSI, JAEA, KAERI, NWMO, NWS, SÚRAO, SSM and Taipower for their financial and technical support of the work described in this paper. The statements made in the paper are, however, solely those of the authors and do not necessarily reflect those of the Funding Organisations. BGS would like to acknowledge the dedicated work of SKB and sub-contractors in making Lasgit a successful field scale experiment at the Äspö Hard Rock Laboratory.

Appendix A

Model comparison

Differences between the proposed numerical strategies lie in conceptual features, the software used by the teams, the assumed geometry to represent the saturated bentonite, the initial/boundary conditions prescribed for the test and in the material parameters. Here, these differences are reported.

Conceptual differences

Table 5
Brief description of the four numerical models developed by the participating teams

	BGR/UFZ	LBNL	CIMNE-UPC/Andra	KAERI
Hydro-mechanical (HM) coupling	Fully coupled (via the Biot's effective stress)	Sequentially coupled (via the Biot's effective stress)	Fully coupled (via the Biot's effective stress)	Fully coupled (via the Biot's effective stress)
Key hydraulic features	Van Genuchten- Mualem model	Van Genuchten- Corey model	Fracture-dependent van Genuchten model/relative permeabilities	Van Genuchten- Mualem model
Mechanical deformation	Elasto-plasticity (Drucker-Prager with a tension cut-off parameter)	Linear elasticity (with swelling stress)	Elasticity (with a dilatancy term in the deviatoric component of the volumetric strains)	Elasto-damage model (damage factor from the minimum principal strain, only tension considered)
Dilatant pathways description	Strain-dependent intrinsic permeability triggered by a heterogeneous Young's modulus	Permeability is assumed to depend on pressure and the effective minimum compressive stress	Intrinsic and relative permeabilities are assumed to be decomposed into matrix and fracture terms	Intrinsic permeability is decomposed into undamaged and damaged terms

Codes

Table 6
Software employed by the participating teams

	BGR/UFZ	LBNL	CIMNE-UPC/Andra	KAERI
Software	OpenGeoSys	TOUGH2 + FLAC3D	CODE_BRIGHT	COMSOL Multiphysics®
Version	5.8	TOUGH2 V2.1 FLAC3D V5	8.6	5.4
Reference	Kolditz et al.[17]	Pruess et al.[24] + Itasca[16]	Olivella et al.[23]	Comsol[4]

Test geometries

Table 7
Test geometries employed by the teams

	BGR/UFZ	LBNL	CIMNE-UPC/Andra	KAERI
Discretisation method	Finite element	Integral finite difference	Finite element	Finite element
Geometry	3D hexahedral mesh (1/4 model)	3D quadrilateral mesh (1/2 model)	3D hexahedral mesh (1/4 model)	3D hexahedral mesh (1/4 model)
Number of elements	21840	37107	66948	9635
Number of nodes	24354	Not provided	13170	Not provided by the software
Material groups	7 (bentonite blocks, swollen bentonite, bentonite interfaces, injection filter, rock, copper wall, cylinder and fractured rock)	7 (bentonite blocks, interfaces, pellets, injection filter, rock, canister, concrete plug)	7 (bentonite blocks, pellets, interfaces, gap bentonite-copper, injection filter, host rock and copper cylinder)	5 (bentonite blocks, bentonite-bentonite interfaces, canister-bentonite interface(void), rock, pellet)

Prescribed initial conditions

Models differ on the assumed material groups considered and thus, we refer to conditions specified in specific subsections (in Section 3).

Prescribed boundary conditions

Models differ on the assumed material groups considered and thus, we refer to conditions specified in specific subsections (in Section 3).

Parameter values

Basic parameters used for the bentonite blocks are the same as the ones used in the modelling of the laboratory scale experiment (see[36]). Main differences are thus in parameters used to describe the interfaces.

Parameters employed by BGR/UFZ

.

Table 8
Parameters employed by BGR/UFZ (coloured in red those assumed or fitted parameters)

Parameter	Symbol [units]	Pre-compacted bentonite		Swelled bentonite	
		Value	Reference	Value	Reference
Cohesive strength	C [MPa]	0.05	Börgesson et al.[3]	0.05	-
Dry density	ρ_s [kg/m^3]	1670	Cuss et al.[5]	1503	-
Friction angle	Φ [°]	10	Börgesson et al.[3]	10	-
Initial saturation	S_0 [-]	0.92	Cuss et al.[5]	0.92	Cuss et al.[5]
Initial void ratio	e_0 [-]	0.66	Cuss et al.[5]	0.8	-
Intrinsic permeability	k_{int} [m^2]	3.4×10^{-21}	Tamayo-Mas et al.[35]	3.4×10^{-21}	Tamayo-Mas et al.[35]
Maximum swelling pressure	$\sigma_{sw,max}$ [MPa]	6.2	Seiphoori[31]	6.2	Seiphoori[31]
Mean gas entry	$\overline{p}_{entry}$ [MPa]	10.6	Seiphoori[31]	4.8	Seiphoori[31]
Mean Young's modulus	$\overline{E}$ [MPa]	307	Tamayo-Mas et al.[35]	276	-
Poisson ratio	ν [-]	0.4	Tamayo-Mas et al.[35]	0.4	Tamayo-Mas et al.[35]

(*continued on next page*)

Table 8 (*continued*)

Parameter	Symbol [units]	Pre-compacted bentonite		Swelled bentonite	
		Value	Reference	Value	Reference
Porosity	ϕ [-]	0.4	Tamayo-Mas et al.[35]	0.44	Tamayo-Mas et al.[35]
Tensile strength	f_t [MPa]	1	-	0.001	-
Strain dependent permeability parameter	b_1 [-]	10000	-	10000	-
	b_2 [-]	250	-	250	-
	b_3 [-]	250	-	250	-
vG parameter	m [-]	0.5	Villar[40]	0.5	Villar[40]
vG parameter	n [-]	2.0	Villar[40]	2.0	Villar[40]

Parameters employed by LBNL

.

Table 9
Parameters employed by LBNL (coloured in red those assumed or fitted parameters)

Parameter	Symbol [units]	Value		Reference
		Bentonite blocks	Interfaces	
Elastic modulus	E [MPa]	307		Tamayo-Mas et al.[35]
Poisson's ratio	ν [-]	0.4		Tamayo-Mas et al.[35]
Porosity	ϕ [-]	0.44		Tamayo-Mas et al.[35]
Biot's coefficient	α [-]	1		Fixed
Swelling coefficient	β_{sw} [-]	0.015		Calibrated
Max aperture for stress-k	b_{ho} [m]	$4.9x10^{-6}$		Calibrated
Reference stress for stress-k	$\sigma_{n,ref}$ [MPa]	0.1		Calibrated
Intrinsic permeability	[m^2]	3.4×10^{-21}	3.4×10^{-20}	Tamayo-Mas et al.[35] for blocks and calibrated for Interfaces
Capillary scaling (capillary pressure)	P_0 [MPa]	18		Senger and Marschall[33]
Shape factor (capillary pressure)	λ [-]	0.45		Senger and Marschall[33]
Residual liquid saturation	Slr [-]	0.01		Senger and Marschall[33]
Residual gas saturation Srg (relative permeability)	S_{rg} [-]	0.13	0.05	Calibrated
Gas permeability enhancement (relative permeability)	m_g [-]	3750		Calibrated

Parameters employed by CIMNE-UPC/Andra

.

Table 10
Parameters employed by CIMNE-UPC/Andra (coloured in red those assumed or fitted parameters)

Parameter	Symbol [units]	Value				Reference
		Rock	Bentonite cylinders and rings	Pellets	Gap	
Elastic modulus	E [MPa]	69000	307			Tamayo-Mas et al.[35]
Poisson's ratio	ν [-]	0.25	0.4			Tamayo-Mas et al.[35]
Initial porosity	ϕ_0 [-]	0.003	0.366	0.706	variable	Damians et al.[8]
Biot's coefficient	α [-]	0.0	0.5			Damians et al.[8]
Dilatancy angle	Ψ [°]	-	24			Damians et al.[8]
Intrinsic reference permeability	k_0 [m^2]	$1x10^{-18}$	$1x10^{-19}$/$1x10^{-20}$/$1x10^{-21}$ (random heterogeneity) $1x10^{-20}$ in the horizontal and vertical contact interfaces		$1x10^{-20}$ / $1x10^{-21}$ / $1x10^{-22}$	assumed
Capillary scaling (capillary pressure)	P_0 [MPa]	0.5	20	0.5	20	assumed
Shape factor (capillary pressure)	Λ [-]	0.3	0.3			Damians et al.[8]
Liquid (relative + intrinsic permeability)	n_l [-]	3	3			Damians et al.[8]
Max./min. liquid saturation (relative permeability)	S_l [-]	1.0/0.0	1.0/0.0			constant
Gas (relative permeability)	n_g [-]	3	2			Damians et al.[8]
Max./min. gas saturation (relative permeability)	S_g [-]	0.3/0.0	0.3/0.0			Damians et al.[8]
Max./min. gas saturation (intrinsic permeability)	S_g [-]	1.0/0.0	1.0/0.0			Damians et al.[8]

(*continued on next page*)

Table 10 (*continued*)

Parameter	Symbol [units]	Value				Reference
		Rock	Bentonite cylinders and rings	Pellets	Gap	
Tortuosity for dissolved gas (Fick's law)		0.5	0.5			Damians et al.[8]
Dispersivity for dissolved gas Longitudinal (Fick's law)		0.5	0.5			Damians et al.[8]
Dispersivity for dissolved gas Transversal (Fick's law)		0.05	0.05			Damians et al.[8]
Specific heat	c_α [J•kg^{-1}•K^{-1}]	750	1091		variable	Damians et al.[8]
Molar mass of helium	M [kg/mol]		0.004			constant
Henry's constant	H [MPa]		1000			Damians et al.[8]

Parameters employed by KAERI

.

Table 11
Parameters employed by KAERI (coloured in red those assumed or fitted parameters)

Parameter	Symbol [units]	Value					Reference
		Void	Bentonite	Interface	Pellet	Rock	
Elastic modulus	E [MPa]	184	307	246	229	60 [GPa]	Bentonite: Tamayo-Mas et al.[35] Others: Calibrated
Density	ρ [kg/m^3]	990	1650	1320	1230	2600	Bentonite: Tamayo-Mas et al.[35] Others: Calibrated
Poisson's ratio	ν [-]	0.4					Tamayo-Mas et al.[35]
Porosity	ϕ [-]	0.64	0.40	0.52	0.55	0.10	Bentonite: Tamayo-Mas et al.[35] Others: Calibrated
Biot's coefficient	α [-]	0.875					Calibrated
Pore compressibility	C_p[1/Pa]	5.11 x 10^{-9}	4.94 x 10^{-9}	4.73 x 10^{-9}	4.77 x 10^{-9}	1.00 x 10^{-11}	Calibrated
Intrinsic permeability	k_{int} [m^2]	2.2 x 10^{-19}	3.4 x 10^{-21}	2.3 x 10^{-20}	4.2 x 10^{-20}	3.7 x 10^{-24}	Bentonite: Tamayo-Mas et al.[35] Others: Calibrated
Capillary scaling (capillary pressure)	P_0 [MPa]	0.70	17.51	3.50	2.25	1.80 x 10^5	Calibrated
Shape factor (capillary pressure)	λ [-]	0.45					Fixed
Shape factor (capillary pressure)	λ_{rel} [-]	3.0					Fixed
Residual liquid saturation	Slr [-]	0.01					Calibrated
Tensile strength	f_t [MPa]	0.001	1.0	0.8	0.001	25.0	Calibrated
Empirical factor (Damage-based permeability)	A [-]	22.2					Calibrated
Experimental rock damage value	D_{kmax} [-]	1					Calibrated
Experimental maximum permeability of the damaged bentonite	k_{max} [m^2]	1.0 x 10^{-18}					Calibrated

Data availability

Data will be made available on request.

References

1. Bandis SC, Lumsden AC, Barton NR. Fundamentals of rock joint deformation. *Int J Rock Mech Mining Sci Geomech Abstr*. 1983;20:249–268. https://doi.org/10.1016/0148-9062(83)90595-8.
2. Biot MA, Willis DG. The elastic coefficients of the theory of consolidation. *J Appl Mech*. 1957;24(4):594–601. https://doi.org/10.1115/1.4011606.
3. Börgesson L, Johannson LE, Sandén T, Hernelind J. *Modelling of the physical behaviour of water saturated clay barriers. Laboratory tests, material models and finite element application*. Stockholm (Sweden): Swedish Nuclear Fuel and Waste Management Co.; 1995.
4. COMSOL. *COMSOL Multiphysics version 5.4a. Manual*. 2018.
5. Cuss R.J., Harrington J.F. and Noy D.J. 2010. Large scale gas injection test (Lasgit) performed at the Äspö Hard Rock Laboratory. Svensk Kärnbränslehantering AB; Stockholm, Sweden.
6. Cuss RJ, Harrington JF, Noy DJ, Graham CC, Sellin P. Evidence of localised gas propagation pathways in a field-scale bentonite engineered barrier system; results from three gas injection tests in the Large scale gas injection test (Lasgit). *Appl Clay Sci*. 2014;102:81–92. https://doi.org/10.1016/j.clay.2014.10.014.
7. Cuss R.J., Harrington J.F., Tamayo-Mas E., Noy D.J., Birchall D.J., Sellin P., and Nord M. 2022. Large scale gas injection test (Lasgit) performed at the Äspö Hard Rock Laboratory. Final report. SKB Technical Report SKB TR-22-06 529pp.
8. Damians IP, Olivella S, Gens A. Modelling gas flow in clay materials incorporating material heterogeneity and embedded fractures. *Int J Rock Mech Mining Sci*. 2020;136, 104524. https://doi.org/10.1016/j.ijrmms.2020.104524.
9. Daniels KA, Harrington JF. The response of compact bentonite during a 1D gas flow test. *Br Geo Survey Open Rep OR/17/067*. 2017.
10. Delage P, Lefebvre G. Study of the structure of a sensitive clay and of its evolution during consolidation. *Can Geotech J*. 1984;21:21–35, 10.1139/t84-003.
11. Harrington JF, Graham CC, Cuss RJ, Norris S. Gas network development in a precompacted bentonite experiment: Evidence of generation and evolution. *Appl Clay Sci*. 2017;147:80–89. https://doi.org/10.1016/j.clay.2017.07.005.
12. Harrington JF, Graham CC, Cuss RJ, Norris S. Gas Network Development in Compact Bentonite: Key Controls on the Stability of Flow Pathways. *Geofluids*. 2019;2019:1–19. https://doi.org/10.1155/2019/3815095.

13. Harrington JF, Horseman ST. *Gas migration in KBS-3 buffer bentonite. Sensitivity of test parameters to experimental boundary conditions. Technical Report TR-03-02.* Stockholm, Sweden: Svensk Kärbränslehantering AB (SKB); 2003.
14. Harrington JF, Milodowski AE, Graham CC, Rushton JC, Cuss RJ. Evidence for gas-induced pathways in clay using a nanoparticle injection technique. *Mineral Mag.* 2012;76(8):3327–3336. https://doi.org/10.1180/minmag.2012.076.8.45.
15. Horseman ST, Harrington JF, Sellin P. Gas Migration in MX80 Buffer Bentonite. *MRS Online Proc Library*. 1996;465:1003–1010. https://doi.org/10.1557/PROC-465-1003.
16. Itasca, Flac3d Version 6.0. *Fast Lagrangian Analysis of Continua in 3 Dimensions*. ITASCA Consulting Group Inc; 2018. ⟨https://www.itascacg.com/software/flac3d⟩.
17. Kolditz O, Bauer S, Bilke L, et al. OpenGeoSys: an open-source initiative for numerical simulation of thermo-hydro-mechanical/chemical (THM/C) processes in porous media. *Environ Earth Sci.* 2012;67(2):589–599. https://doi.org/10.1007/s12665-012-1546-x.
18. Levasseur S., Collin F., Daniels K., Dymitrowska M., Harrington J., Jacops E., Kolditz O., Marschall P., Norris S., Sillen X., Talandier J., Truche L. and Wendling J. 2021. Initial State of the Art on Gas Transport in Clayey Materials. Deliverable D6.1 of the HORIZON 2020 project EURAD, Work Package Gas. EC Grant agreement no: 847593.
19. Levasseur S., Collin F., Dymitrowska M., Harrington J., Jacops E., Kolditz O., Marschall P., Norris S., Sillen X., Talandier J., Truche L. and Wendling J. 2024. State of the Art on Gas Transport in Clayey Materials – Update 2023. Deliverable D6.2 of the HORIZON 2020 project EURAD, Work Package Gas. EC Grant agreement no: 847593.
20. Levasseur S., Collin F., Dymitrowska M., Harrington J., Jacops E., Kolditz O., Marschall P., Norris S., Sillen X., Talandier J., Truche L. and Wendling J. 2024. State of the Art on Gas Transport in Clayey Materials – Update 2023. Deliverable D6.2 of the HORIZON 2020 project EURAD, Work Package Gas. EC Grant agreement no: 847593.
21. Noghretab BS, Damians IP, Olivella S, Gens A. Coupled hydro-gas-mechanical 3D modeling of LASGIT experiment. *Geomech Energy Environ.* 2024;40, 100623. https://doi.org/10.1016/j.gete.2024.100623.
22. Olivella S, Alonso EE. Gas flow through clay barriers. *Geotechnique*. 2008;58:157–168. https://doi.org/10.1680/geot.2008.58.3.157.
23. Olivella S, Gens A, Carrera J, Alonso EE. Numerical formulation for a simulator (CODE_BRIGHT) for the coupled analysis of saline media. *Eng Comput*. 1996;13(7):87–112. https://doi.org/10.1108/02644409610151575.
24. Pruess K, Oldenburg CM, Moridis G. *TOUGH2 User's Guide, Version 2.1, LBNL-43134 (revised)*. Berkeley, California: Lawrence Berkeley National Laboratory; 2012.
25. Radeisen E, Shao H, Hesser J, Kolditz O, Xu W, Wang W. Simulation of dilatancy-controlled gas migration processes in saturated bentonite using a coupled multiphase flow and elastoplastic H2M model. *J Rock Mech Geotech Eng.* 2023;15(4):803–813. https://doi.org/10.1016/j.jrmge.2022.05.011.
26. Rutqvist J. Status of the TOUGH-FLAC simulator and recent applications related to coupled fluid flow and crustal deformations. June 2011 *Comput Geosci*. 2011;37(6):739–750. https://doi.org/10.1016/j.cageo.2010.08.006.
27. Rutqvist J. An overview of TOUGH-based geomechanics models. *Comput Geosci*. 2017;108:56–63. https://doi.org/10.1016/j.cageo.2016.09.007.
28. Rutqvist J. Modeling gas migration through clay-based buffer material using coupled multiphase fluid flow and geomechanics with stress-dependent gas permeability. *Geomech Energy Environ.* 2025;41, 100627. https://doi.org/10.1016/j.gete.2024.100627.
29. Rutqvist J, Ijiri Y, Yamamoto H. Implementation of the Barcelona Basic Model into TOUGH-FLAC for simulations of the geomechanical behavior of unsaturated soils. *Comput Geosci*. 2011;37:751–762. https://doi.org/10.1016/j.cageo.2010.10.011.
30. Rutqvist J, Wu Y-S, Tsang C-F, Bodvarsson GA. Modeling approach for analysis of coupled multiphase fluid flow, heat transfer, and deformation in fractured porous rock. *Int J Rock Mech Mining Sci*. 2002;39:429–442. https://doi.org/10.1016/S1365-1609(02)00022-9.
31. Seiphoori A. 2015. Thermo-Hydro-Mechanical Characterisation and Modelling of Wyoming Granular Bentonite. Nagra. Nagra Technical Report 15-05; Wettingen, Switzerland.
32. Sellin P, Leupin OX. The use of clay as an engineered barrier in radioactive-waste management a review. *Clays Clay Minerals*. 2013;61:477–498. https://doi.org/10.1346/CCMN.2013.0610601.
33. Senger R. and Marschall P. 2008. Task Force on EBS/Gas Transport in Buffer Material, NAGRA NAB 08-24, Wettingen, Switzerland, 2008.
34. Senger R, Romero E, Marschall P. Modeling of gas migration through low-permeability clay rock using information on pressure and deformation from fast air injection tests. *Transp Porous Media.* 2018;123:563–579. https://doi.org/10.1007/s11242-017-0962-5.
35. Tamayo-Mas E, Harrington JF, Brüning T, et al. Modelling advective gas flow in compact bentonite: lessons learnt from different numerical approaches. *Int J Rock Mech Mining Sci.* 2021;139(104580). https://doi.org/10.1016/j.ijrmms.2020.104580.
36. Tamayo-Mas E, Harrington JF, Damians IP, et al. Advective gas flow in bentonite: Development and comparison of enhanced multi-phase numerical approaches. *Geomech Energy Environ.* 2024;37, 100528. https://doi.org/10.1016/j.gete.2023.100528.
37. Tamayo-Mas E, Harrington JF, Damians IP, Olivella S, Radeisen E, Rutqvist J, Wang Y. Advective gas flow in bentonite: Development and comparison of enhanced multi-phase numerical approaches. *Geomech Energy Environ.* 2024;37, 100528. https://doi.org/10.1016/j.gete.2023.100528.
38. Tang CA, Tham LG, Lee PKK, Yang TH, Li LC. Coupled analysis of flow, stress and damage (FSD) in rock failure. *Int J Rock Mech Min Sci*. 2002;39(4):477–489. https://doi.org/10.1016/S1365-1609(02)00023-0.
39. van Genuchten MT. A closed-form equation for predicting the hydraulic conductivity of unsaturated soils. *Soil sci society Am j*. 1980;44(5):892–898. https://doi.org/10.2136/sssaj1980.03615995004400050002x.
40. Villar M.V. 2005. MX-80 Bentonite. Thermo-Hydro-Mechanical Characterisation Performed at CIEMAT in the Context of the Prototype Project. Departamento de Impacto Ambiental de la Energía, Vol. 1053. Informes Técnicos CIEMAT: 45; Madrid, Spain.
41. Xu W, Shao H, Hesser J, Wang W, Kolditz O, Popp T. Simulation of dilatancy-controlled gas migration process in saturated argillaceous rock. *Comput Geomech COMGEO II - Proc 2nd Int Symp Comput Geomech.* 2011:693–703.